Feasibility Study of a Linear Generator Wave Energy Converter With Adaptive Bistable Control

by

Alexander Wunderlich
B.S. Virginia Polytechnic Institute and State University (2010)
M.E.M. Old Dominion University (2021)

Submitted to the Department of Mechanical Engineering
in partial fulfillment of the requirements for the degrees of
Engineer's Degree in Naval Architecture and Marine Engineering
and
Master of Science in Mechanical Engineering
at the
MASSACHUSETTS INSTITUTE OF TECHNOLOGY
June 2023

Author .....
Alexander Wunderlich
Department of Mechanical Engineering
May 18, 2023

Certified by .....
Paul Sclavounos
Professor of Mechanical Engineering and Naval Architecture
Thesis Supervisor

Accepted by .....
Nicolas Hadjiconstantinou
Chairman, Department Committee on Graduate Theses

Feasibility Study of a Linear Generator Wave Energy Converter With Adaptive Bistable Control

by

Alexander Wunderlich

Submitted to the Department of Mechanical Engineering
on May 18, 2023, in partial fulfillment of the
requirements for the degrees of
Engineer's Degree in Naval Architecture and Marine Engineering
and
Master of Science in Mechanical Engineering

Abstract

Oceanic wave energy harvesting is a promising source of renewable energy that involves the conversion of oscillatory motion into electrical energy. However, the majority of traditional wave energy converters rely on intermediary mechanisms that increase complexity and can incur energy losses. Linear generators have emerged as a promising wave energy technology that bypass the limitations of intermediaries through direct mechanical to electrical energy conversion. The convention is to configure the generator so that incident waves excite the resonant frequency of the device. The irregular and broadband nature of ocean waves poses a challenge to this technique, as the device must be configured to respond to a wide range of incident frequencies. This thesis proposes a novel design for a linear permanent magnet generator that considers a tension leg platform oscillating in oceanic surge motion as its basis. The performance of the proposed device is analyzed using numerical simulations, and the potential for optimization techniques and the implementation of adaptive bistable control logic to improve broadband energy harvesting is investigated. The results demonstrate that these proposed alterations can increase the harvesting potential and efficiency of a wave energy converter, with the potential to contribute to the growing demand for renewable energy sources.

Thesis Supervisor: Paul Sclavounos
Title: Professor of Mechanical Engineering and Naval Architecture

Acknowledgments

Completion of this research and my three years in the Naval Construction and Engineering Program would not have been possible without the help and support of many individuals I would like to acknowledge. First and foremost, I would like to thank my thesis advisor, Professor Paul Sclavounos. Professor, you were able to adeptly balance the art of providing me sufficient guidance to keep me moving forward, while advising and teaching me in a manner that was just above my academic level such that I would rise to the occasion, all while evaluating me and setting expectations in a way that minimized negative stress. Advising me in this way simultaneously made this project enjoyable and an incredible learning experience, which can be a difficult thing to find these days.

I would also like to thank the other student working in my lab, Lucas Stone. Although you claim to have minimal computer skills, your grasp of mathematics and sheer determination helped you make enough progress with modeling and simulation that I was forced to turn to you for help when I got stuck; for this I am forever grateful and indebted to you.

To my 2N class of 2023, we leaned heavily on each other during the dark days of Psets, and I thank you for helping me through them. I look forward to seeing you all again in my fine US Navy, which I'd also like to thank for giving us 2N students this incredible opportunity at MIT.

Last but not least, I would like to thank my family. To my parents and sisters, thank you for your encouragement and putting up with my military career. To my wonderful wife, Christiana, who does not see stress in any situation, leading to life being an endless party. To my daughter, Velzy May, thank you for entering my life during thesis crunch time. Because you are absolutely perfect in every way, raising you has been no challenge at all and life has actually become easier since you've arrived.

Contents

List of Figures

List of Tables

Chapter 1

Introduction

This thesis studies the implementation of a novel active control strategy to improve the efficiency of a Linear Permanent Magnet Generator (LPMG). The LPMG is designed and scaled for use in an ocean wave energy converter (WEC) in the form of a tension leg platform (TLP) point absorber. Chapters 2 and 3 review fundamental technology and present a theoretical model configuration for consideration. Chapters 4, 5, and 6 provide a proposed control strategy, the predicted power output of the device, and a conclusion.

1.1 Motivation

Rapid technological advancements over the past several decades coupled with the steady rise in human population have led to a commensurate demand for increased electrical power generation on a global scale. Presently, 80% of these demands are met by carbon dioxide emitting, fossil fuel sources [3, 10]. Global warming and the associated negative environmental impacts are attributed to a rise in atmospheric carbon dioxide levels. These issues have already shaped today's culture by reaching a status of climate crisis and will only worsen if the trend continues.

The most recent United Nations Climate Change Conference aimed to address alarming climate trends with ambitious targets to secure global net zero carbon emissions by mid-century, and curtail global warming to less than 1.5 C degrees [10,

11]. Some efforts outlined by this conference include accelerating the phase-out of coal, increasing the use of electric vehicles, and encouraging investment in renewable energy sources [10,11]. All solutions suggest a significant increase in electrical power demands that will largely be met by alternative sources free of carbon dioxide emissions. By 2035 fossil fuels reliance is expected to drop to 60%, with alternative energy sources covering the substantial remainder [3]. Today's alternative energies are primarily composed of solar, wind, and hydro, but are expected to incorporate additional innovative technologies as global climate change efforts continue. One of the most promising renewable energy sources is oceanic wave energy due to its high power density, high efficiency, and recent technological improvements [3, 12–14].

1.2 Prospect of ocean wave energy

When compared with most renewable power sources, harvesting energy from ocean waves is a relatively immature industry. Commercial photovoltaic installations began generating power in the 1950s and hydromechanical energy capture predates the steam engine, however, most test and commercial installations of ocean wave energy did not begin until the turn of the century. Ocean waves boast a power density of 2 to 3 kW/m^2, which is approximately two times higher than solar energy, and three times higher than wind power, while all three sources maintain comparable capacity factors of 20% to 35%, depending on location [2]. Estimates predict that the global ocean wave energy capacity is between 1-10 TW, or 8,000 to 80,000 TW·hr/yr. This is the highest power generation potential when compared to other renewable sources and is on the same order of magnitude of global energy consumption [2,3,13–15]. With this promising outlook, wave energy can augment future renewable energy production to levels required of ambitious sustainability goals. To achieve these goals current WEC technology must improve efficiency, operability, and manufacturability to ensure that rapid growth of the industry is economically feasible. Figure 1-1 depicts annual mean wave power spanning a 10-year period; it is noted that a WEC's productivity can drastically change depending on the installation site location.

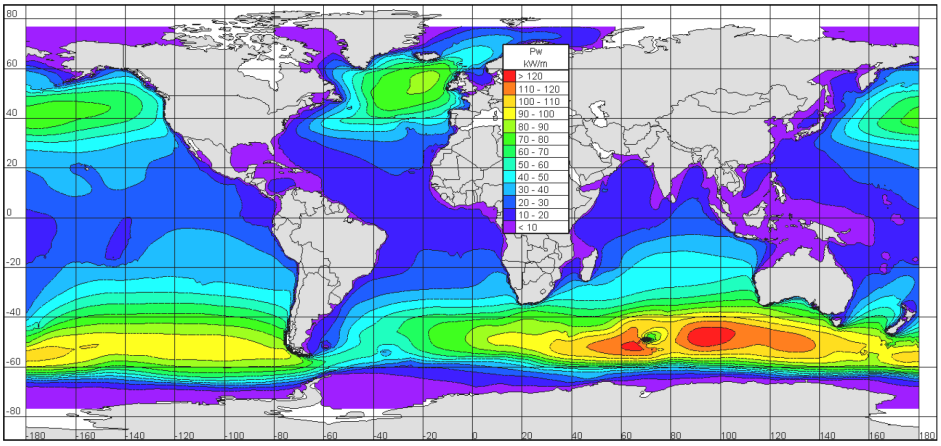

Figure 1-1: Global distribution of annual mean wave power [1].

A hurdle to the wave energy industry that must not be overlooked is the harsh operating conditions that a WEC must withstand. The device must be designed to tolerate a corrosive environment in addition to extreme forces during worst-case sea state scenarios. A majority of recent WEC technologies aim to minimize moving parts and complicated operations to overcome these challenges. The added benefit of this trend is reduced maintenance requirements that translate to both operational cost savings and an increase in feasible fetch length [3]. As the wave energy industry develops, rapid scaling will likely be impeded by opposition, similar to those faced by the offshore wind industry. This includes concerns regarding ocean bottom disturbance, visibility from the coastline, impeded access to fishing areas, and obstructed commercial traffic. Regulatory agencies, like the U.S. Environmental Protection Agency, will require specific mitigating measures to compensate for these impacts.

1.3 Scope and framework

To conduct a practical feasibility study, the theoretical installation site will be the United States coastlines in the New England region. Throughout their development, WECs have evolved to incorporate a diverse range of designs for harvesting ocean energy, including oscillating water columns, hydraulic pumps, rotating machines, and direct energy converters. A literature review was conducted to determine the

preferred WEC device and Power Takeoff Mechanism (PTO) to be analyzed as a strong candidate for further improvement with the implementation of control strategies. This review is discussed in chapters 2 and 3. The selected device is a TLP point absorber WEC with a direct energy LPMG PTO consisting of Halbach array permanent magnets. Although arguably better PTOs or LPMG topologies may exist, this is not an optimization study and will primarily investigate theoretical power generation and a novel control strategy to improve the efficiency of existing LPMG technology. A relatively small PTO will be considered so it may be cost-effectively manufactured in high quantity and have a wide range of applications. This PTO could be employed on smaller WECs that provide a power source for unmanned vehicle charging or small-scale emergency power generation, but for the purpose of this study, the case of a single PTO placed in a TLP point absorber will be considered. Although the designed TLP could be applied in large-scale energy production, wave farm optimization and multiple TLP interaction effects are considered outside the scope of this study.

Chapter 2

Fundamentals of Wave Energy Converters and Ocean Modeling

A WEC serves as the interface to extract energy from incident periodic ocean waves. These devices can be classified into several categories, most commonly based on their principles of operation. A PTO then serves as a method to convert this mechanical power to electricity to be later discussed in Chapter 3. This chapter serves as a review of WECs and concludes with the methods used to model incident ocean waves.

2.1 Wave Energy Converters

Wave Energy Converter devices harvest ocean energy by capturing mechanical power from accelerations in the vertical heave, horizontal surge, or less frequently rotational pitch directions. This linear or rotational motion is then converted to electricity by either driving a turbine or employing direct energy conversion. The most common processes of electrical generation used today are outlined in figure 2-1. The types of WEC devices existing today can be classified as an overtopping device, oscillating water column (OWC), or point absorber.

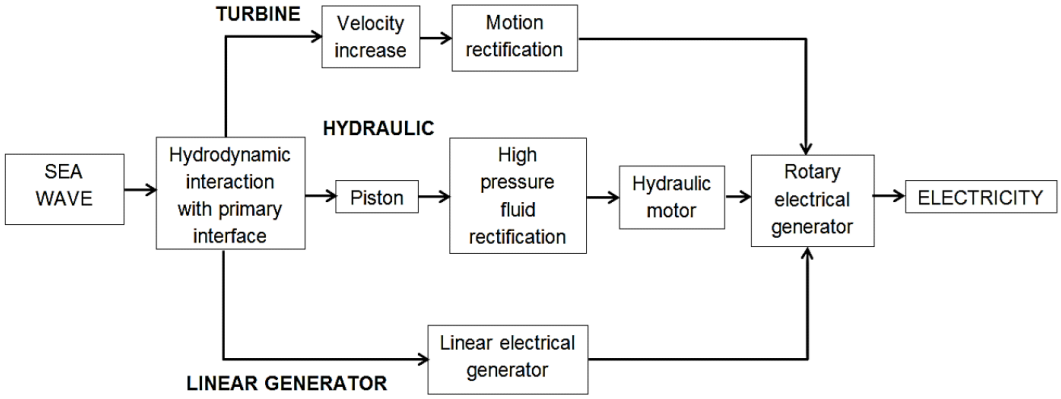

Figure 2-1: Working processes of WEC devices [2].

2.1.1 Overtopping device

An Overtopping device is comprised of a large reservoir structure that allows seawater to flow over the sides from ocean wave action. As the reservoir seawater rises, a pressure head is created to drive a rotating turbine for electrical power generation. These devices have successfully been tested, including the Wave Dragon and the Sea-wave Slot-cone Generator, and have realized efficiencies between 25% and 30%. [3, 14]. The advantage of these structures is that steady electrical power can be generated, assuming the reservoir remains full. Additionally, these devices can be made large enough to produce several MW of power and could be placed in shallow, coastal regions to also serve a breakwater function [3, 14].

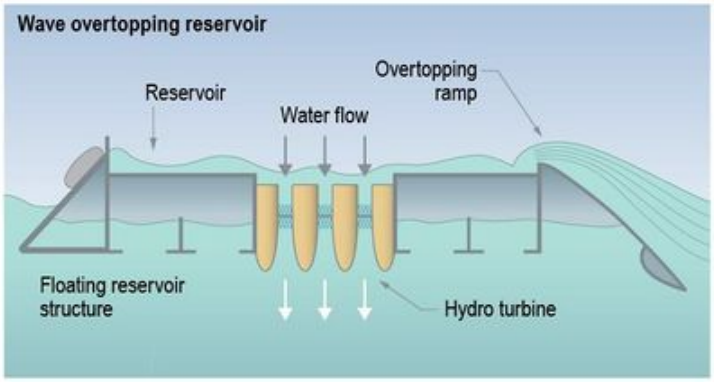

Figure 2-2: Overtopping WEC device [3].

2.1.2 Oscillating Water Column device

The OWC operates on the principle of utilizing the time-varying pressure field that is created within a chamber due to incident ocean wave crests and troughs, to operate an air or hydraulic driven turbine generator. Most OWC WECs employ a pneumatic design to simplify the device and increase the longevity of the sensitive mechanical components by only exposing them to air [3, 14]. Although theoretical efficiencies of an OWC WEC can reach over 80%, experimental results have been greatly hindered by high moisture content in the air [3, 14].

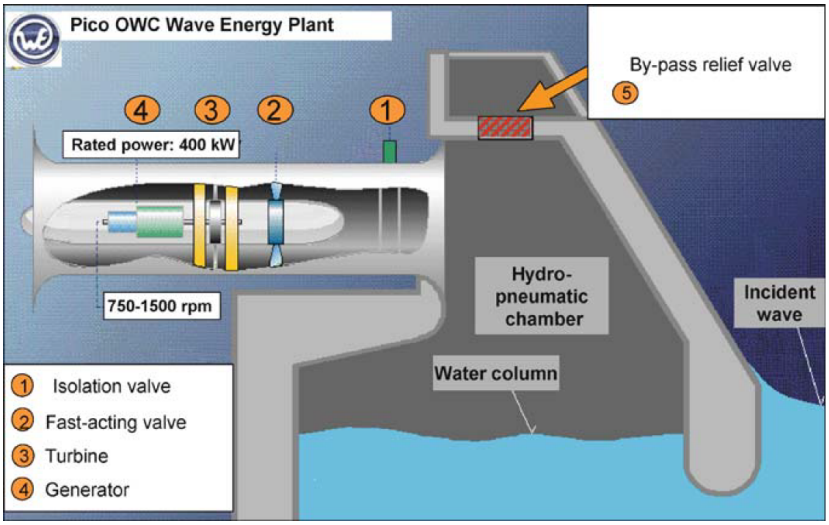

Figure 2-3: Pico OCW power plant [4].

The OCW power plant seen in figure 2-3 illustrates a 400 kW pneumatic turbine that was built on the island of Pico, Azores, Portugal. The Islay LIMPET power plant in the United Kingdom employs this same construction but is slightly larger, rated at 500 kW. Both plants operated intermittently throughout a period of 20 years and have since been decommissioned. Although successful, these turbines were plagued with maintenance issues due to the harsh operating conditions inherent to the ocean environment [3, 4].

2.1.3 Point absorber device

A majority of recent WEC research has focused on point absorber devices due to their versatility, cost-effectiveness, and high power density [3]. These devices are typically small relative to the wavelength of the incident waves and are most often designed to oscillate with ocean surface heaving motion. Some heaving designs have a second submerged body that captures energy from the relative motion between the two bodies. The most popular examples of this arrangement are the Archimedes Wave Swing (AWS) and the Uppsala University Lysekil Spar, both of which have been successfully tested with full-scale prototypes [3, 16]. These devices capture energy from the relative motion by employing a vertical linear generator to directly produce electrical power.

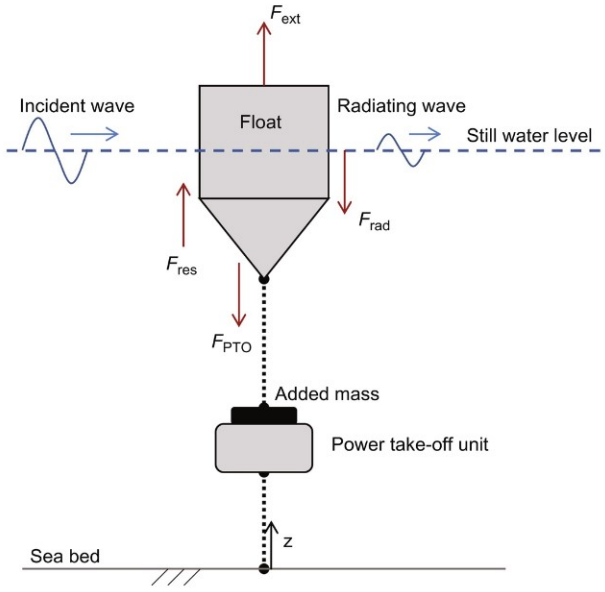

Figure 2-4: Two body, heaving point absorber WEC [5].

Alternate point absorber WEC devices have been designed to capture motion from other degrees of freedom, such as linear surge motion, or surge coupled with rotational pitch motion. A point absorber can be studied similarly to vibration theory, where damping, restoring, and external forces acting on the body create oscillating motion that will be further discussed in section 2.2.2.

2.2 Ocean Wave modeling and hydrodynamic forces

To maximize the energy harvesting potential of a WEC, the incident ocean waves must be accurately represented, and the resulting wave-body interaction with the WEC must be fully understood. In effort to model a realistic ocean environment, this study assumes fully developed, irregular waves in deep water that are numerically simulated using stochastic processes.

2.2.1 Ocean wave spectra

In the event that regular periodic waves are experienced by a WEC device, modeling is straightforward, and energy extraction is maximized by tuning the natural frequency of the device to that of the incident waves. In reality, oceanic waves are irregular and are a product of complex interactions with wind and the ocean surface. Wind generated waves begin developing linearly with a two-dimensional spectral structure, and then develop over time non-linearly through absorption of energy from the wind. High frequency components gradually saturate through breaking waves as their steepness exceeds a physical limit or by nonlinear wave-wave interaction, while low frequency components continue to grow and become less irregular (known as swell); this develops a wave energy spectrum with a spectral peak that is partial to lower frequencies [17, 18].

Beginning with a time history set of one-dimensional wave records at a certain ocean location, $x(t)$, that is defined as a steady-state, ergodic, random process, let $X(\omega)$ represent this time history in the frequency domain through the Fourier transform of $x(t)$. The spectral density function of this wave record for a given period T is then defined as follows:

$$S_{xx}(\omega) = \lim_{T\to\infty} \frac{1}{2\pi T} \mid X_T(\omega) \mid^2 \tag{2.1}$$

The definition in equation 2.1 may then be broadened to the three-dimensional case comprised of the wave-number vector k, through the Wiener-Khinchin theorem and

the auto-correlation function, to arrive on the frequency spectrum of a homogeneous wave field that is irrespective of wave direction. The full derivation is described by Ochi [17].

Representing fully developed seas as a spectral density function was first popularized by Pierson and Moskowitz in 1962 [17,19]. Other spectrum models, such as JONSWAP, Bretschneider, and ISSC models, are commonly used in the design of offshore structures. Varying models may accurately represent the same energy content, but distribute it differently across the frequency band. Thus, in the design of a WEC, where performance is largely dependent on the frequency of the incident waves, model selection can lead to widely varying results. The most appropriate selection to represent the New England ocean environment in this study is the fully developed Bretschneider model, defined by equation 2.2.

$$S(\omega) = \frac{5}{16}\frac{\omega_m^4}{\omega^5}H_{\frac{1}{3}}^2 e^{\frac{-5\omega_m^4}{4\omega^4}} \tag{2.2}$$

$H_{\frac{1}{3}}$ Significant wave height

ω_m Modal frequency

The continuous wave spectrum seen in equation 2.2 may be discretized to aid in computation. The number of frequency bins selected to approximate the spectrum as a Riemann sum should be high enough to ensure that a trusted simulation can be produced without periodicity concerns, specifically, the size of the bins should be $\Delta\omega = \frac{2\pi}{T}$. With a time period, T, selected to be 310 seconds, and frequency range ω_{min} - ω_{max} of 0.5 - 3.5 radians/s, we determine that the number of frequency bins, N, is 148. A representation of the discretized spectral density used in this study is depicted in figure 2-5. A significant wave height of 3.3m and a period of eight seconds are assumed to simulate sea state code 5 (rough seas) for WEC response analysis.

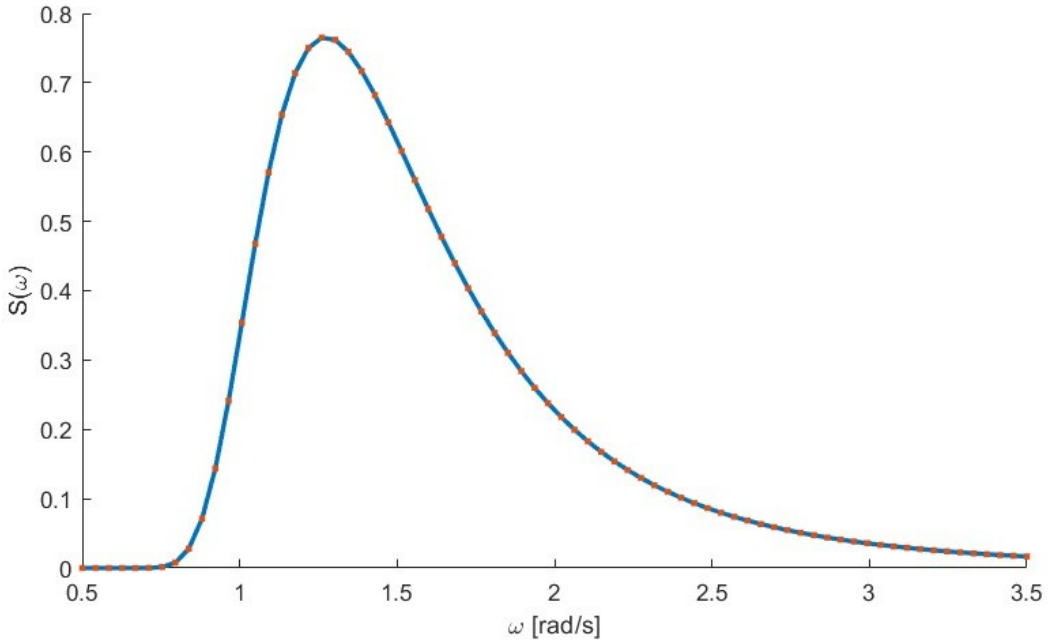

Figure 2-5: Discretized Bretschneider spectrum using 148 frequency bins for significant wave height of 3.3m and period of 8 seconds.

With the relationship between spectrum and wave amplitude, A_k, shown in equation 2.3, the wave elevation signal in equation 2.4 can be generated by randomly selecting θ_k phase values.

$$A_k = \sqrt{2S(\omega_k)\Delta\omega_k} \tag{2.3}$$

$$\zeta(t) = \sum_{k=1}^{N} A_k cos(\omega_k t + \theta_k) \tag{2.4}$$

An example signal generated in this manner is seen in figure 2-6; randomized time history samples such as this will be employed to simulate incident waves during this study.

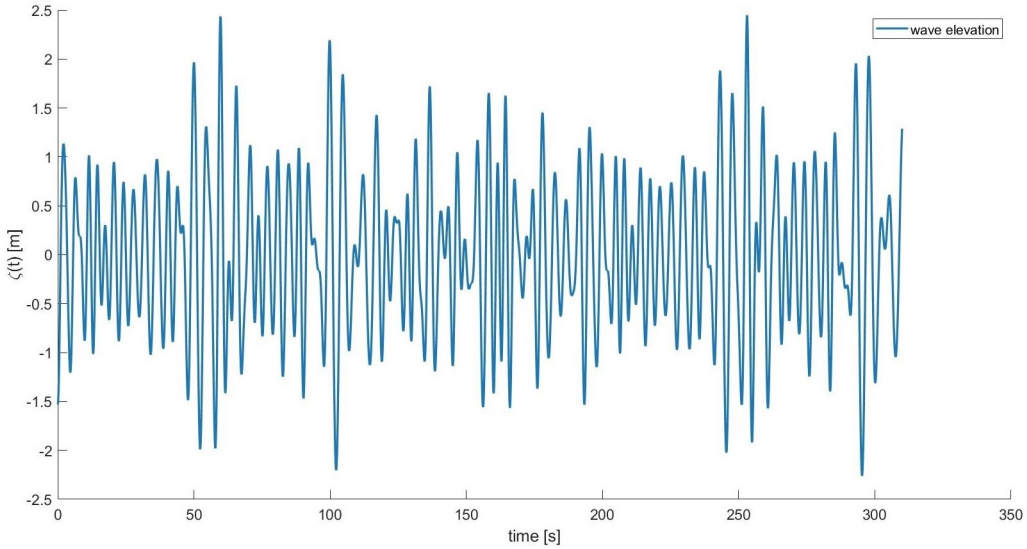

Figure 2-6: Simulated wave elevation signal from a discretized Bretschneider spectrum over a period of 310 seconds (trial 1).

To verify that this function was generated properly and that the time period evaluated is sufficient in length, a Fast Fourier Transform (FFT) was taken of the generated signal and it corresponds well with the expected Bretschneider spectrum, as seen in figure 2-7.

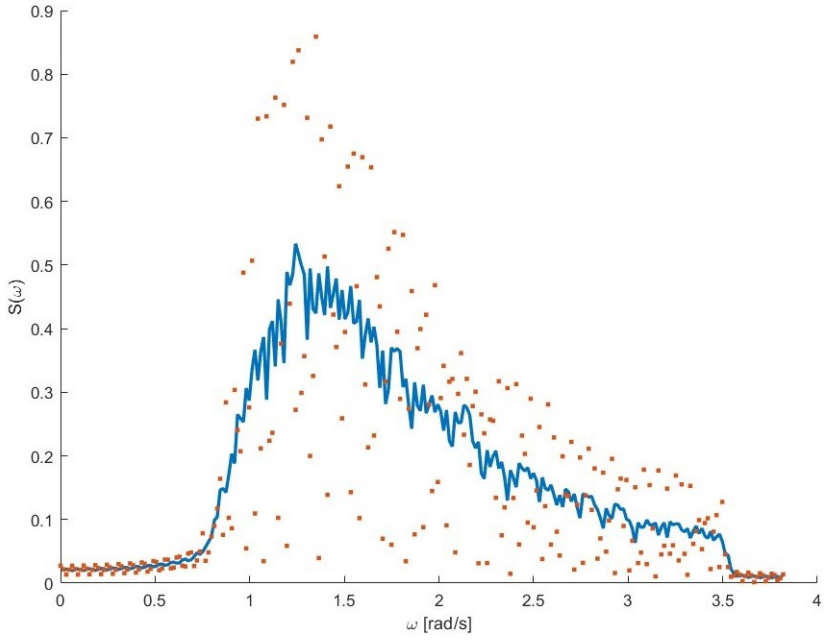

Figure 2-7: FFT of 310 second time history generated signal (trial 1).

2.2.2 Hydrodynamic forces

A point absorber WEC device floating on the ocean's free surface will experience various forces that together describe the wave-body interaction. These forces include diffraction, radiation, Froude-Krylov, hydrostatic, viscous damping, and gravity forces. For convenience, the non-viscous forces can be determined using Haskind relations of exciting forces and moments from direct integration of hydrodynamic pressure. With this approach, the 6x6 linear system seen in equation 2.5 is obtained through application of Newton's law. This equation describes wave-body interaction in the frequency domain for 6 Degrees of Freedom and provides the resultant, frequency dependent, complex amplitude of the body's motion, also known as the Response Amplitude Operator (RAO).

$$\sum_{j=1}^{6}[-\omega^2(M_{ij}+A_{ij})+i\omega(B_{ij})+(C_{ij}+C_{ij}^{E})]\mathbb{I}_j = X_i \tag{2.5}$$

ω	Angular frequency
M_{ij}	Body mass and inertia matrix
A_{ij}	Added mass coefficient
B_{ij}	Damping coefficient
C_{ij}	System hydrostatic and gravitational restoring coefficient
C_{ij}^{E}	External restoring coefficient
$\mathbb{I}_j$	Response Amplitude Operator for TLP
X_i	Exciting forces from the Haskind relations

These values are a function of the WEC geometry and incident frequency, and can be calculated from wave interaction software to be discussed in section 3.1.3.

Chapter 3

Proposed Wave Energy Converter Specifications and Modeling

When considering design configurations for a WEC device, the full life cycle must be considered. Designs that are too large or complex can lead to a costly installation. Further, environmental concerns may arise if the installation and operations are intrusive. Required routine maintenance should be minimized to reduce operational costs, while longevity must also be considered for a device being deployed in the harsh ocean environment. For these reasons, a TLP with an LPMG for the Power Take Off mechanism is selected. This chapter details the proposed device to be investigated, as well as the modeling methods used for analysis.

3.1 Tension Leg Platform

The TLP concept was first popularized in the 1980s during cost-saving measures in the offshore oil and gas industry that led to the development of tethered floating platforms [18]. These devices are heave restrained by vertical tendons that reduce set-down, while remaining compliant in horizontal modes of motion.

3.1.1 Tension Leg Platform description

The TLP considered as the basis for the WEC in this study is depicted in figure 3-1, and has been investigated by MIT Laboratory for Ship and Platform Flows.

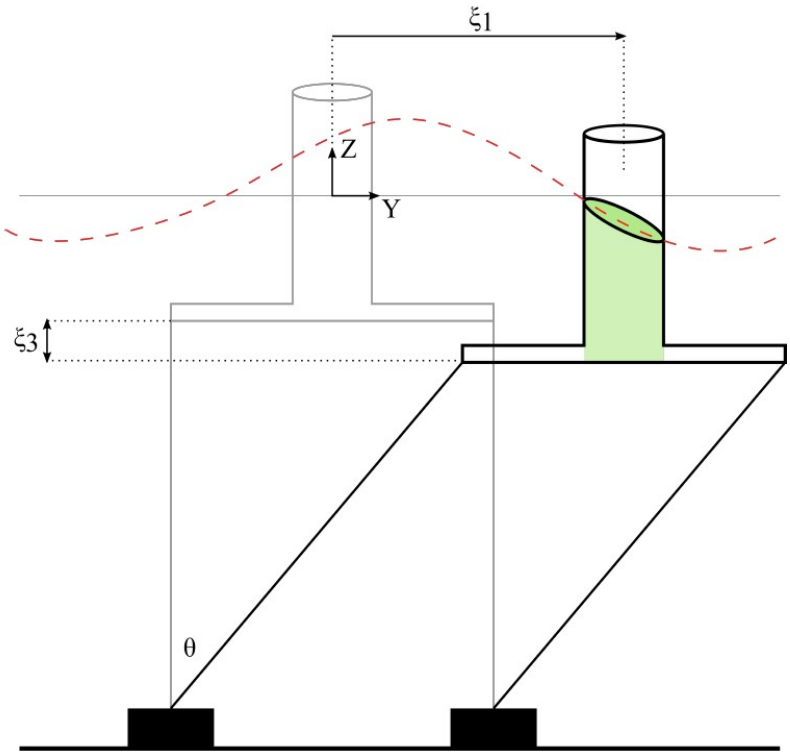

Figure 3-1: TLP with a horizontal displacement ξ_1 and a set-down ξ_3 [6].

The tendons and associated attachment arms are slender structures with small volumes relative to the cylindrical buoy and are therefore neglected with respect to hydrodynamic forces. The heave, pitch, and roll responses of a TLP are precluded through the vertical restraints, except at resonance where the response lies primarily on the tendon tension. Due to the dynamic restoring mechanism of the tendons and geometry of the buoy, the TLP naturally mitigates excessive wave loads via horizontal compliance, which aids in promoting longevity. In the case of a stiff offshore system, the low natural period can lead to concerns in response to high frequency excitation forces (such as ringing loads), which could lead to high tendon load response [18]. When considering these challenges, the selection of tendon pretension becomes of great interest, as the design should also aim to maximize the desired horizontal motion

that promotes energy capture at lower frequencies.

The TLP geometry should be selected such that it remains small relative to the incident wavelength to validate the point absorber assumption, but it also must remain large enough that overall mass is substantial relative to the LPMG, allowing for the inertial effects of the oscillating PTO to be neglected. With these considerations, the description of the selected TLP comprised of a slender cylinder is described in table 3.1.

Table 3.1: TLP WEC particulars.

Diameter[m]	8
Draft [m]	10
Cylinder height [m]	15
Mass[tonnes]	100

3.1.2 Tension Leg Platform response motion

The PTO is oriented horizontally in effort to capture energy from the large surge acceleration of the TLP, making this the primary mode of concern. With this PTO orientation, and with other modes of motion insignificant in comparison to surge, the TLP equation of motion from 2.5 is simplified to one degree of freedom for surge motion as follows.

$$\begin{aligned} \mathbb{I}_1(\omega) &= \frac{X_1}{-\omega^2(M_{11}+A_{11})+i\omega(B_{11})+(C_{11}+C_{11}^E)} \\ &= |\,\mathbb{I}_1(\omega)\,|\; e^{i\phi(\omega)} \end{aligned} \tag{3.1}$$

All values required to determine surge RAO will be provided by wave interaction software and discussed in the following section, with the exception of the external restoring coefficient from the tendons in surge, C_{11}^E. The value for C_{11}^E should be selected to maximize energy capture, therefore should be selected such that the natural frequency of the system, ω^*, coincides with the peak modal frequency of the incident wave spectrum, ω_m, to improve the likelihood of resonance.

$$
\begin{aligned}
&C_{11}^{E} = \omega^{*2}(M_{11} + A_{11}^{*}) \\
&with \quad \omega^{*} = \omega_m
\end{aligned}
\tag{3.2}
$$

With surge ROA defined, incident wave elevation $\zeta(t)$ from equation 2.4 can be used to determine TLP response motion in surge, ξ_1, as follows.

$$
\begin{aligned}
&\xi_1(t) = \zeta(t)\mathbb{I}_1(\omega) \\
&\xi_1(t) = \sum_{k=1}^{N} A_k \mid \mathbb{I}_1(\omega_k) \mid cos(\omega_k t + \theta_k + \phi_k)
\end{aligned}
\tag{3.3}
$$

3.1.3 Tension Leg Platform modeling

WAMIT (WaveAnalysisMIT) Version 5.4 is a radiation/diffraction panel software developed to analyze complex wave-body interactions. This software solves the linear boundary-value problem with integral equations using a three-dimensional panel method to determine fluid velocity potential and pressure on the body surface [20]. The resulting solution provides various hydrodynamic parameters, which in this study will be applied to describe TLP response motion from incident waves.

To verify WAMIT convergence, two different methods were employed to generate a surface mesh for the cylinder described in table 3.1. First, 30 meshes were built with a structured quadrilateral grid using a MATLAB script with 300 through 2000 panels. The second method employed Rhinoceros 3D modeling software to automatically generate a polyhedral mesh from a NURBS surface with the desired geometry using the QuadRemesh command; again, 30 meshes with 300 through 2000 panels were generated. WAMIT convergence issues were identified for meshes with less than 450 panels, and above this number of panels, results correlated within 0.1% for the two mesh generation methods.

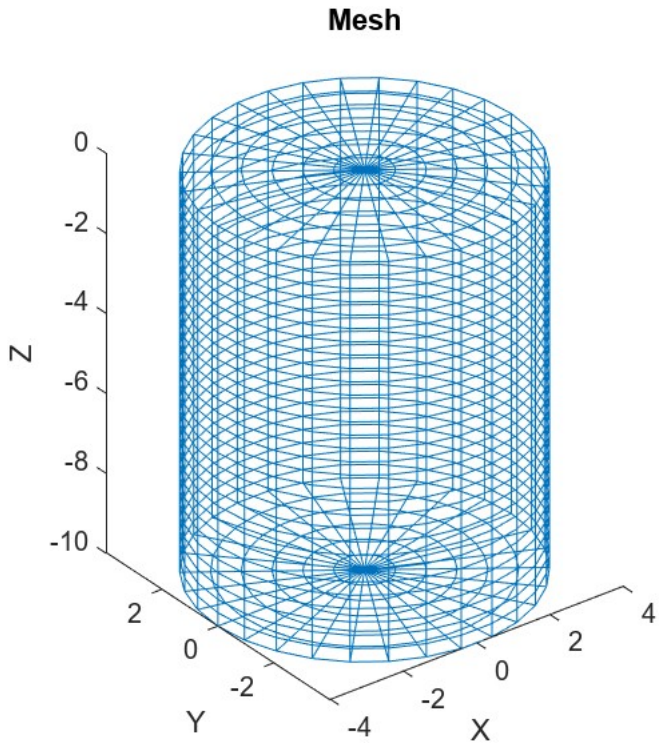

Figure 3-2: MATLAB generated WAMIT mesh with 1260 panels.

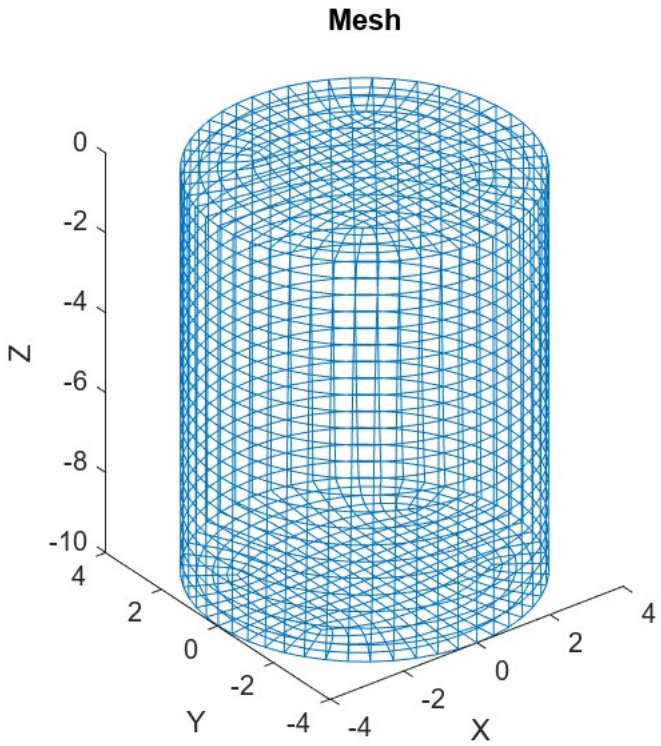

Figure 3-3: Rhinoceros 3D generated WAMIT mesh with 1500 panels.

A WAMIT run was performed for each mesh, using 148 frequency bins, while considering only one incident wave heading, with a deep water assumption. The runs were configured to output added mass, damping coefficient, exciting force from Haskind relations, and phase. The top four images seen in figure 3-4 represent the response parameters for the selected TLP geometry; these results are used in calculations throughout the remainder of the study.

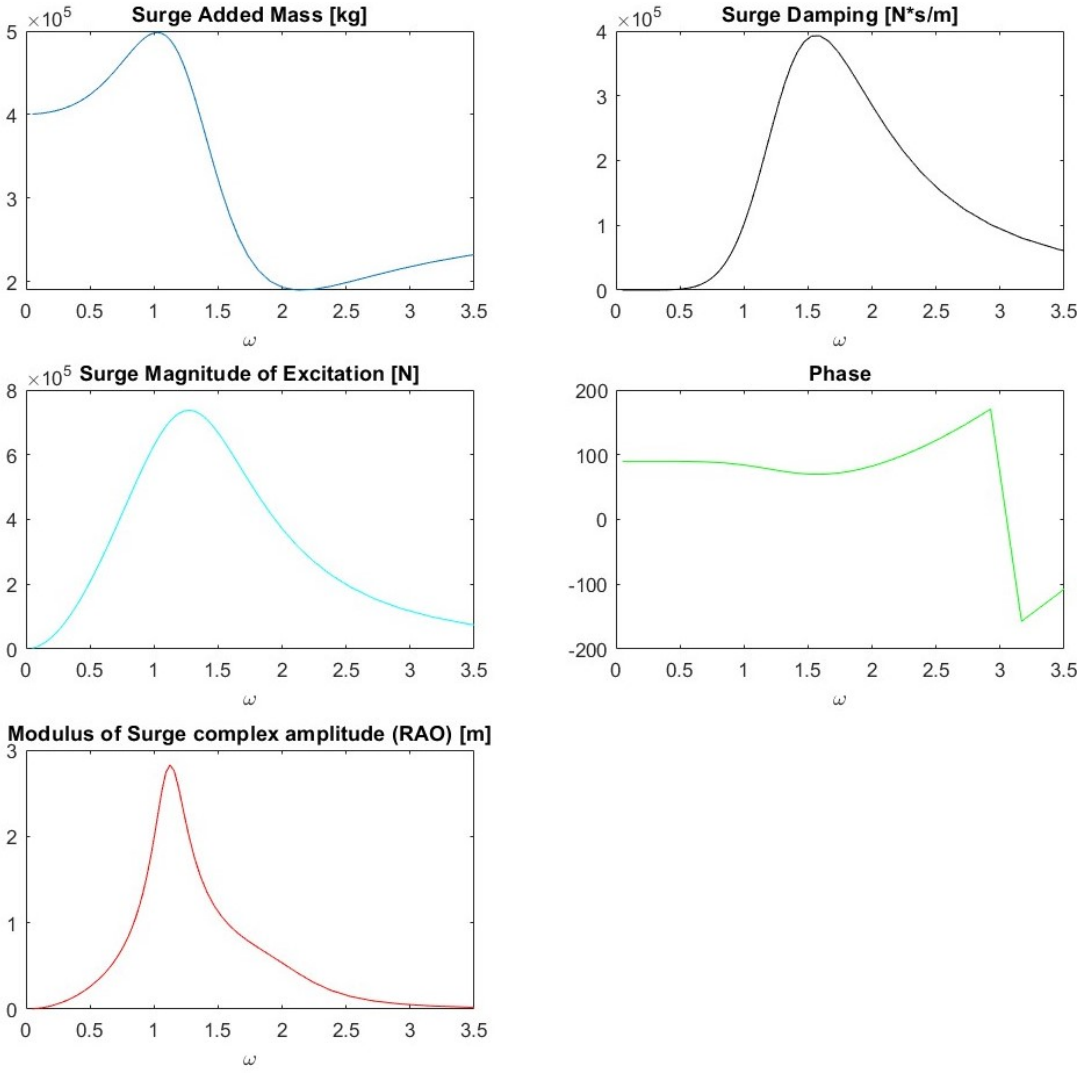

Figure 3-4: WAMIT TLP response parameters.

By inspection of the excitation force, the modal frequency occurs at 1.27 radians/s, corresponding as expected with the eight second modal frequency of the input Bretschneider spectrum. With the peak added mass result from the WAMIT simulation, the mooring lines can be tuned in surge, as described in equation 3.2, to provide an external restoring coefficient of $C_{11}^{E} = 9.37 \cdot 10^{5} \frac{N}{m}$. This result and the response TLP parameters were used to derive the surge RAO, in accordance with equation 2.5, that is displayed in the bottom left of figure 3-4. This RAO can be used to determine TLP body motion using the example wave elevation signal from figure 2-6 and equation 3.3. An example simulated TLP response signal generated in this manner is provided in figure 3-5.

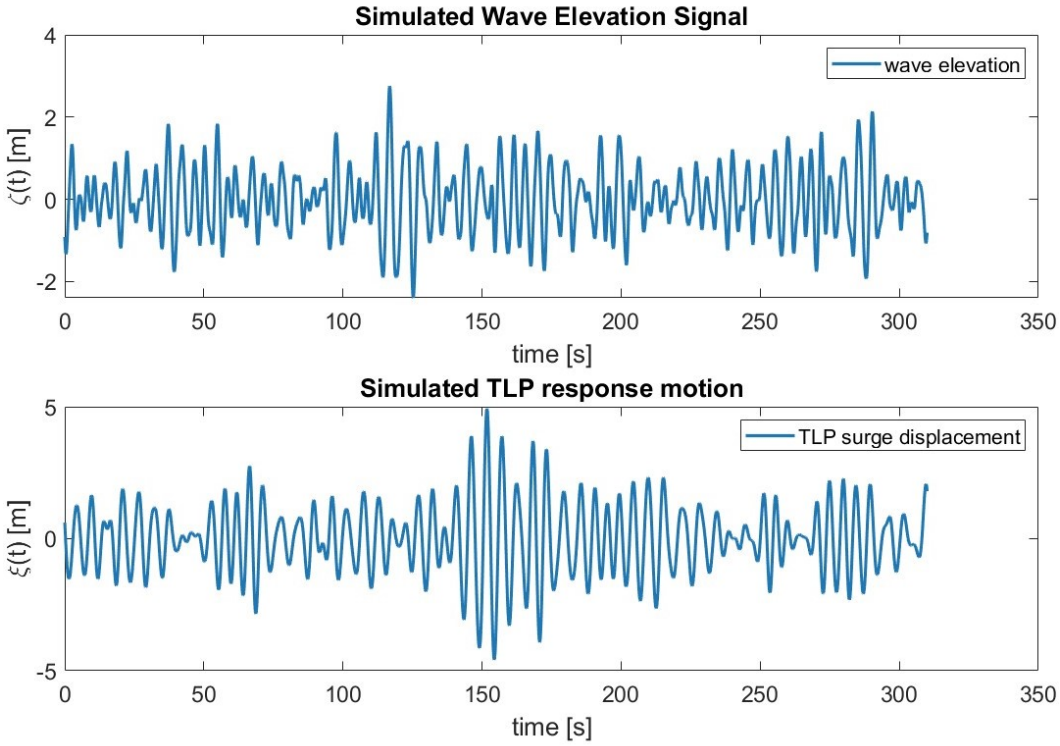

Figure 3-5: TLP response motion due to an incident wave time history, calculated using RAO.

3.2 Power Take Off mechanism

A point absorber WEC may employ a variety of PTO configurations for energy harvesting. Direct energy conversion using an LPMG was considered favorable for this study due to its simplicity, high efficiency, and ability to fully isolate the mechanical assembly from the harsh ocean environment.

3.2.1 Linear Permanent Magnet Generator overview

An LPMG is comprised of an oscillating mass, or "translator" that is magnetically coupled with an armature winding to directly convert translating heave or surge motion to electrical energy. This design is simple yet robust, eliminating losses in intermediaries and requiring no mechanical linkages; as a result, it promotes longevity and requires minimal maintenance. These generators can be designed with a high force-to-weight ratio and its direct-drive operating principle has been proven to result in the highest efficiency among all WEC configurations [2, 13]. For this reason, the LPMG has successfully been incorporated in several prototypes or fully active WECs. Examples include the previously mentioned AWS, a 2 MW rated WEC deployed in 2004 that captures relative heave motion between two bodies using an LPMG, and the 10 kW rated Oregon State University L10 with a similar working principle [3, 7, 14].

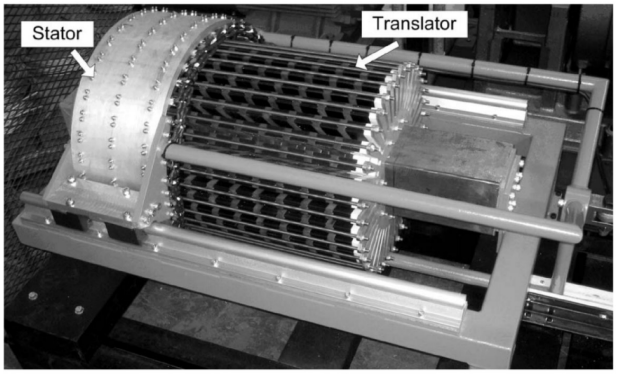

Figure 3-6: Oregon State University L10 WEC [7]

An LPMG may be configured flat or tubular; although the flat arrangement may be favorable in terms of manufacturing, the tubular counterpart is often selected due to its higher force-to-weight ratio, more symmetrical distribution of magnetic flux density throughout the air gap, and lower cogging force [2, 13, 14, 21, 22].

3.2.2 Linear Permanent Magnet Generator topology

The permanent magnets and windings of an LPMG may be arranged such that either remains stationary. Additionally, either may be configured with a short or long geometry relative to the full length of translation. The selected configuration ultimately becomes an optimization problem with respect to both efficiency and manufacturing cost.

In recent years, research has focused on improving LPMG performance through magnetization pattern, coil winding, and loss reduction. To create the steep magnetic flux variation required to generate electrical potential, magnet poles may be arranged axially, radially, or in a Halbach array pattern. Studies have shown that axial polarization has fallen out of favor due to the interaction between poles and stator teeth leading to excessive cogging forces and associated vibrations [8, 21–24]. Figure 3-7 displays the radial and Halbach array polarization patterns.

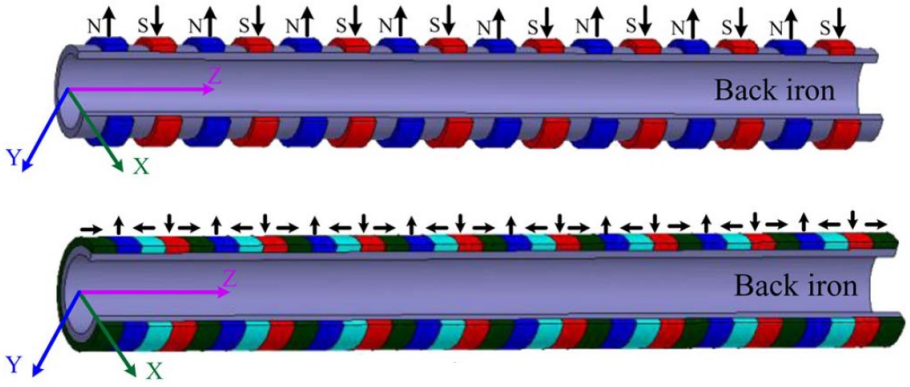

Figure 3-7: LPMG translator with radial (upper) and Halbach (lower) magnet array structure [8]. Note: coordinate system in this image differs from this study.

An advantage of the Halbach array is that the magnetic flux can be directed

outward radially due to its self-shielding magnetization, mitigating the risk of inward flux interacting with ferrous material that may be used to support the translator. When compared to radial, the Halbach array has been proven to reduce cogging force and improved sinusoidal electromotive force (EMF), but has the drawback of higher fabrication cost and complexity [7, 13, 23].

Optimization studies have been performed on three-phase LPMG coil winding arrangement to increase efficiency through improved flux linkage and reduced EMF harmonics and cogging force. Pole or slot pitch, slot teeth, and winding placement, are all parameters that may be varied to achieve improved performance. Figure 3-8 depicts these parameters and several layouts.

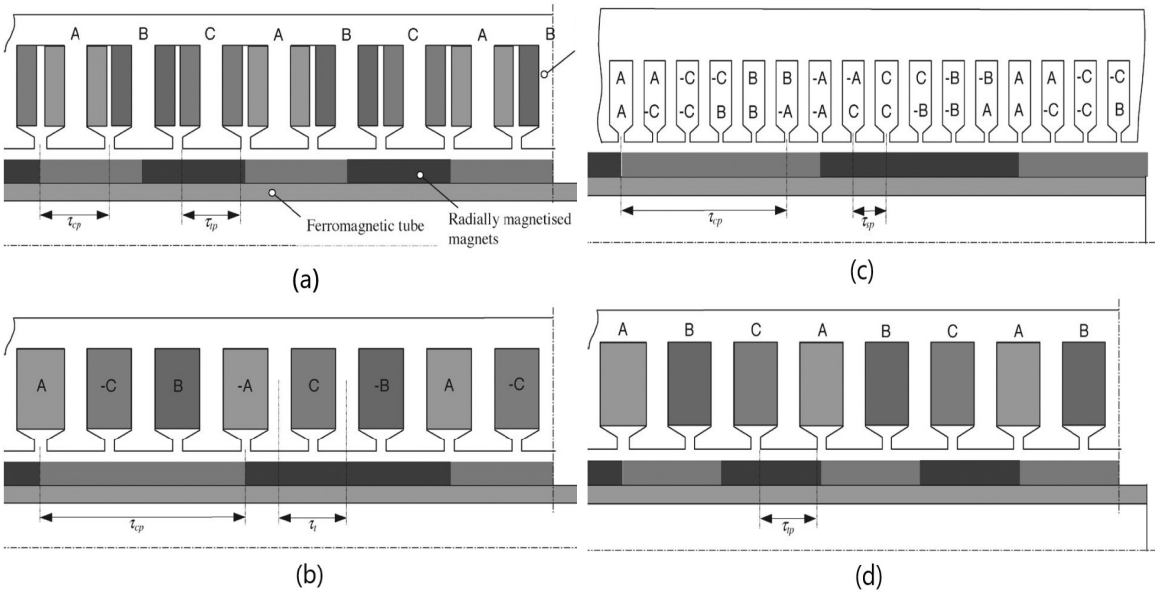

Figure 3-8: Radially magnetized LPMG showing various coil winding configurations. (a) DC winding with two coils per pole per slot. (b) AC winding with one slot per pole per phase. (c) AC winding with two slots per pole per phase. (d) AC winding with one slot per pole-pair per phase [9].

In general, the incorporation of slotted coil winding has been shown to improve flux density and power factor, but with the drawbacks of higher cogging force and eddy current losses within the iron teeth [21]. Cogging force occurs by virtue of

a magnetic pole's propensity to align with the slotted iron teeth, even in the open circuit case. Minimization of this interaction is desirable to reduce machine vibration that can slow translating velocity or damage the device. Several studies aim to reduce cogging force by skewing the orientation of the permanent magnets with promising results; a 30-degree skew will only mildly reduce flux linkage, while cogging force can be reduced by up to 90% [25, 26]. Comparable cogging force reduction with minimal loss to flux linkage has also been achieved using fractional pole pitch length relative to coil pitch; this strategy does not add the complexity involved with manufacturing and assembling a skewed permanent magnet [27, 28].

3.2.3 Proposed design

The LPMG configuration selected for this study features a tubular geometry with a long stator relative to the translator's length. The translator is comprised of a Halbach array, with bonded NdFeB N42 permanent magnets, arranged on an internal armature with a fractional pole pitch that is 91.3% the length of the coil pitch. The stator features a three-phase, AC machine, with one slot per pole-pair per phase. Each phase consists of six coils in series per winding, and slotted coil teeth with pole shoes were incorporated to increase air gap flux density [28, 29]. The pole shoes feature beveled edges to reduce cogging, while the stator ends are also beveled in effort to reduce end effects [28, 29]. The Halbach array features a semi-iron core for back iron benefits, while the stator employs an external back iron, both have been shown to aid in flux shaping and improve working efficiency of the generator [21]. Table 3.2 provides further details regarding the LPMG particulars, figure 3-9 shows 2D axisymmetric views of the LPMG, and figure 3-10 displays a 3D cutaway image.

Table 3.2: LPMG particulars.

Translator mass [kg]	300
Translator stroke length [m]	2
Halbach array length [mm]	123.3
Coil pitch τ_{cp} [mm]	60
Pole pitch τ_p [mm]	54.8
Air gap [mm]	5

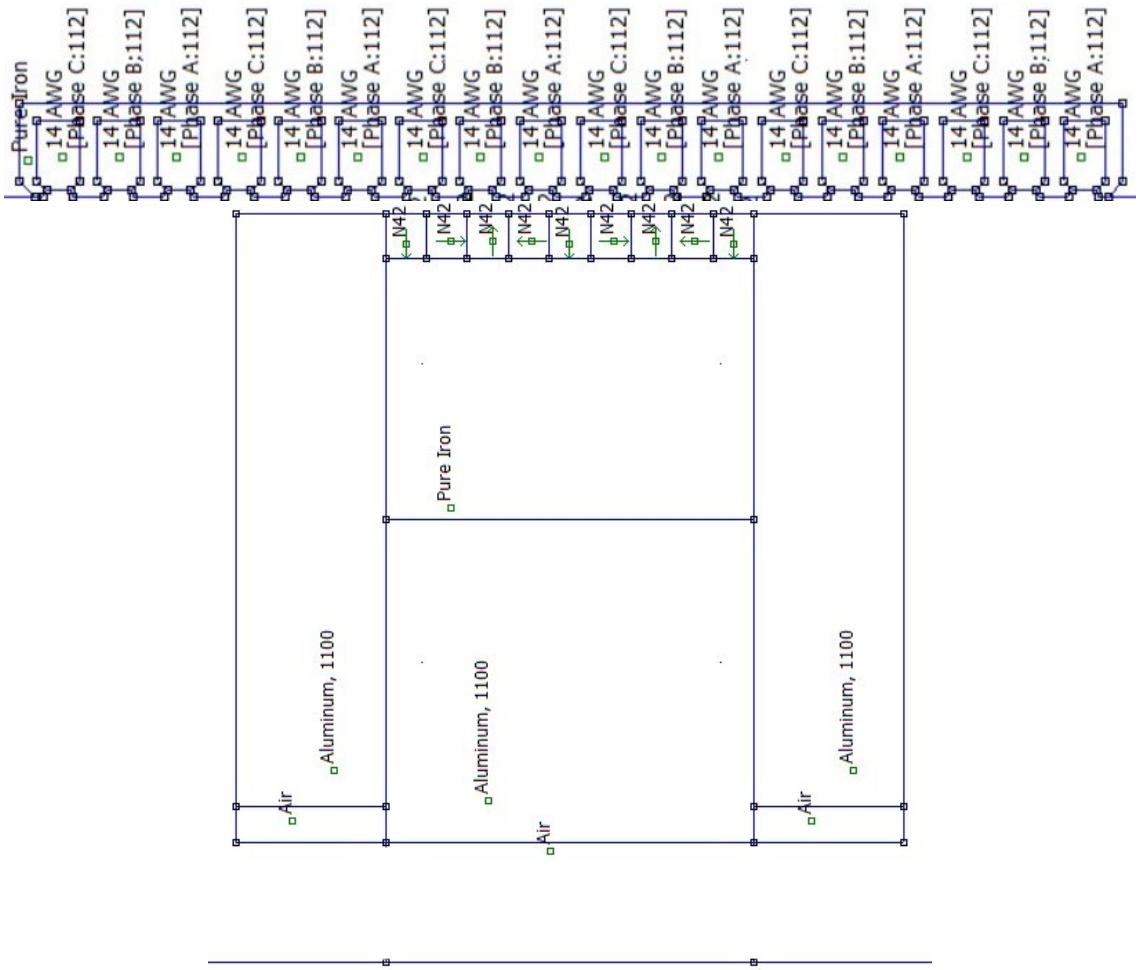

Figure 3-9: 2D axisymmetric diagram of the proposed LPMG design.

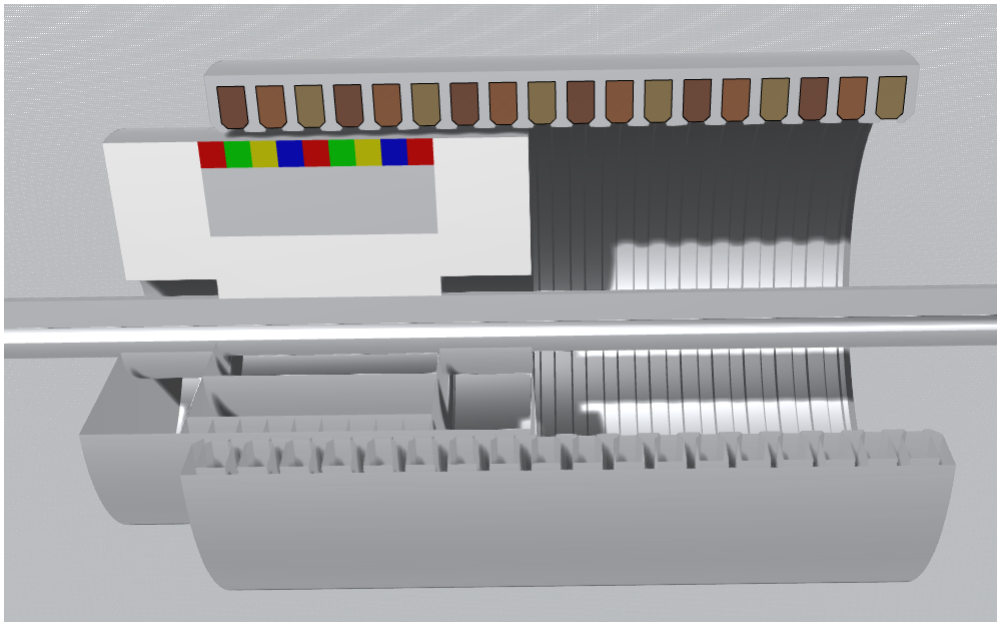

Figure 3-10: 3D model of the proposed LPMG with 90-degree cutout to reveal internals. Colors indicate magnetic polarity of the Halbach array, and shades of copper coil indicate phase winding.

3.2.4 Linear Permanent Magnet Generator analytical model

To accurately predict the energy harvested from induced EMF of the LPMG, motion of the translator and coupling between the translator and stator must be modeled. Displacement of the translator relative to the TLP can be approximated by the linear equation of motion in equation 3.4. This closed form expression for relative translator motion combines the TLP response to incident waves, with the LPMG axial motion to provide a coupled RAO that describes translator response to incident waves.

$$
\begin{aligned}
x(t) &= \mathbb{R}\{\mathbb{X}(\omega)e^{i\omega t}\} \\
[-\omega^2 m + i\omega(b_C + b_L)]\mathbb{X}(\omega) &= \omega^2\, m\, \mathbb{I}_1(\omega) \\
\mathbb{X}(\omega) &= \underbrace{\frac{\omega^2\, m}{[-\omega^2 m + i\omega(b_C + b_L)]}}_{\mathbb{H}(\omega)}\, \mathbb{I}_1(\omega)
\end{aligned} \tag{3.4}
$$

$x(t)$	Translator displacement relative to TLP motion in time domain
ω	Angular frequency
m	Translator mass
b_C	Parasitic damping due to coil resistance
b_L	Useful damping from load resistance
$\mathbb{X}(\omega)$	Coupled TLP and LPMG translator product RAO
$\mathbb{I}_1(\omega)$	Response Amplitude Operator of the TLP in surge
$\mathbb{H}(\omega)$	Transfer function of translator

With both the RAO of the TLP and the transfer function of the translator defined, the translator motion is determined from incident wave amplitude using the complex, combined product RAO, $\mathbb{X}(\omega)$, as follows.

$$
x(t) = \sum_{k=1}^{N} A_k \, |\mathbb{X}(\omega_k)| \, cos(\omega_k t + \theta_k + \phi_k) \tag{3.5}
$$

It is noted that the frictional and viscous damping are not represented in equation 3.4. These contributions to damping are considered negligible since a low friction or a magnetically levitated LPMG is a feasible assumption, and at low speeds viscous effects of air are trivial.

The remaining unknown parameters are b_C and b_L. These values must be determined by linking mechanical motion with EMF, ϵ, through the use of a magnetic coupling coefficient, γ. This coefficient is simply the position derivative of flux linkage, and is derived with Faraday's law as follows.

$$\epsilon = -N_C \frac{d}{dt}\phi_B = -N_C \frac{d\phi_B}{dx(t)}\frac{dx(t)}{dt} = \gamma \dot{x}(t) \tag{3.6}$$

N_C	Number of turn's per winding coil
ϕ_B	Flux linkage between translator and winding
$x(t)$	Translator displacement relative to TLP motion in time domain
$\gamma = -N_C \frac{d\phi_B}{dx(t)}$	Magnetic coupling coefficient

The load resistance, R_L, is determined by the selected WEC power storage circuitry and will be treated as a known and adjustable parameter in this study. With 14 AWG copper wire at N_C turns per each of the four coils in series, the coil resistance per phase, R_C, becomes a function of coil diameter, D_C, and wire resistance per length, Ω.

$$R_C = 4\pi D_C \Omega_{14AWG} N_C \tag{3.7}$$

Finally, using Ohm's law, the current flow through the in-series coil and load circuitry is determined. This current will induce a damping force from the PTO that opposes the translator's direction of motion in accordance with Lenz's law, which is used to derive the damping coefficients as follows.

$$\begin{aligned}
\epsilon = IR_{total} = I(R_C + R_L) &= \gamma \dot{x}(t) \\
I &= \frac{\gamma}{(R_C + R_L)}\dot{x}(t) \\
F_{PTO} &\equiv \gamma I \\
F_{PTO} &= \frac{\gamma^2}{(R_C + R_L)}\dot{x}(t) \\
F_{PTO} \equiv b_T \dot{x}(t) &= (b_C + b_L)\dot{x}(t) \\
b_T &= \frac{\gamma^2}{(R_C + R_L)}
\end{aligned} \tag{3.8}$$

It is noted that the force contribution from the self inductance of the coils is negligible at low frequencies, and thus is omitted from equation 3.8. With an expression for b_T, [30] states that optimal power harvesting occurs with $R_C = R_L$, thus $b_C = b_L$, allowing us to derive a simplified expression for b_L, and in turn, power harvested by the PTO.

$$\begin{aligned} b_L = \frac{b_T}{2} = \frac{\gamma^2}{2(R_C + R_L)} = \frac{\gamma^2}{4R_C} \\ P_{PTO} = F_{Load}\dot{x}(t) \\ P_{PTO} = b_L\dot{x}(t)^2 \end{aligned} \tag{3.9}$$

3.2.5 Finite Element Method Magnetics modeling

The magnetic interaction between stator and translator of an LPMG is complex and difficult to accurately model using analytical methods due to factors such as leakage flux, fringing, and edge effects within the generator. Therefore, Finite Element Method Magnetics (FEMM) software is used to model this interaction throughout this study. The proposed design for the LPMG is modeled using a magnetostatic, axisymmetric problem with a Dirichlet boundary condition. This FEMM model was previously displayed in figure 3-9, and an example mesh, along with the magnetostatic solution are displayed in figure 3-11.

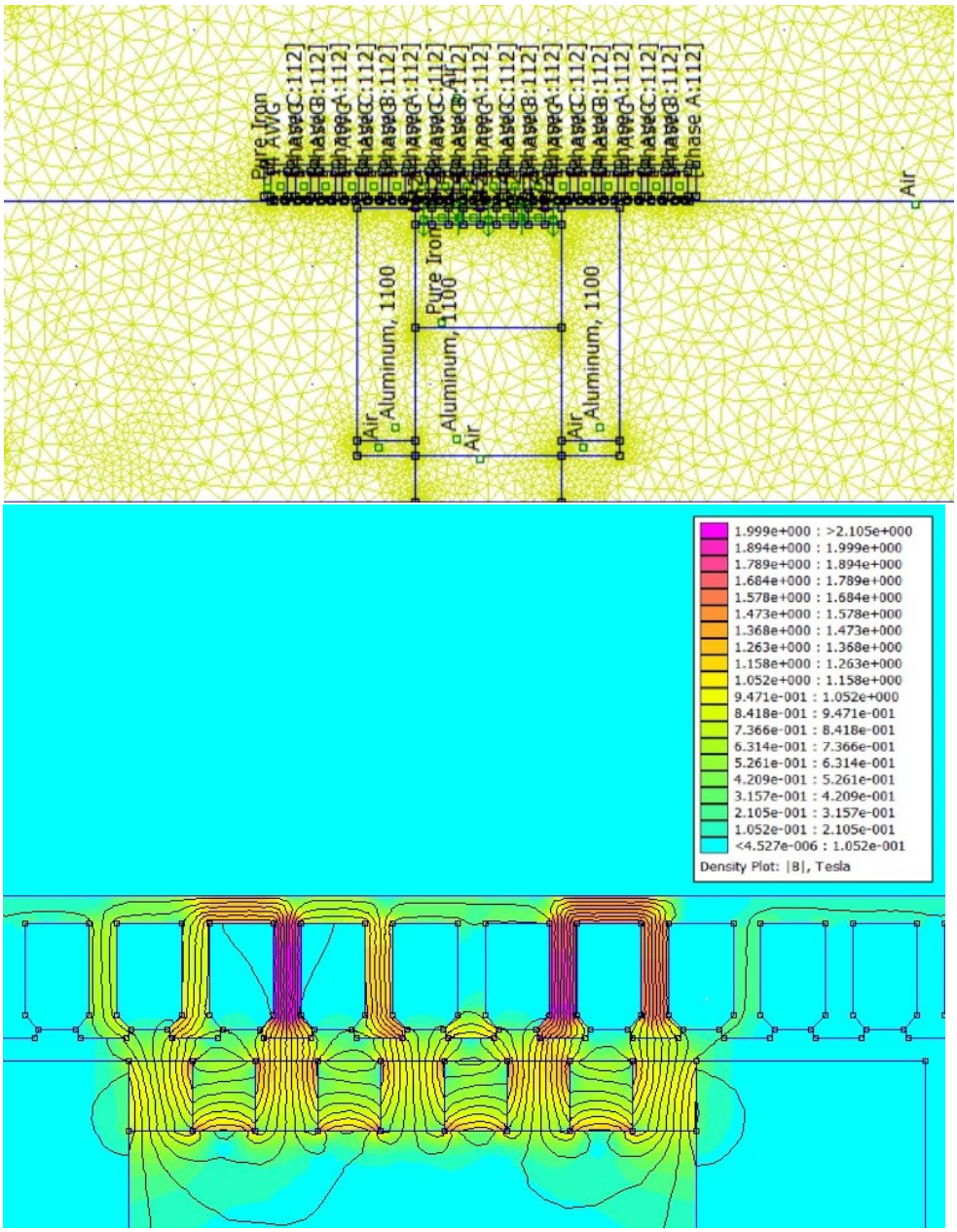

Figure 3-11: Axisymmetric diagram with example mesh for use in the FEMM solver (top). FEMM problem solution with translator at the center position (bottom), this image illustrates the pole shoes and slot teeth focusing the magnetic field to a peak 2 Tesla magnitude.

Since the FEMM software is only able to solve for the static condition, a Lua script was written to simulate motion along the full stroke of the translator using one millimeter step increments. Each step requires the generation of a new mesh and solving of a new magnetostatic problem. For each step increment, the parameters of flux linkage for each phase winding, and the axial force on the translator were calculated. This Lua script is provided in Appendix A.

The flux linkage (which inherently considers the number of turns per coil within the FEMM software) can then be converted to a magnetic coupling coefficient, then damping coefficient, as described in equation 3.4. The results of this process, for each phase winding, are provided in figure 3-12.

The stator circuitry in this study is assumed to take the AC signal from the LPMG and rectify each phase, then only select the phases with peak power to send to the load. With this assumption, we use the RMS value of the peaks to find that the machine has an approximately constant total damping coefficient, b_T, of 3500 Ns/m. This damping value can easily be tuned if desired by reducing flux linkage, and will be further discussed in chapter 4.

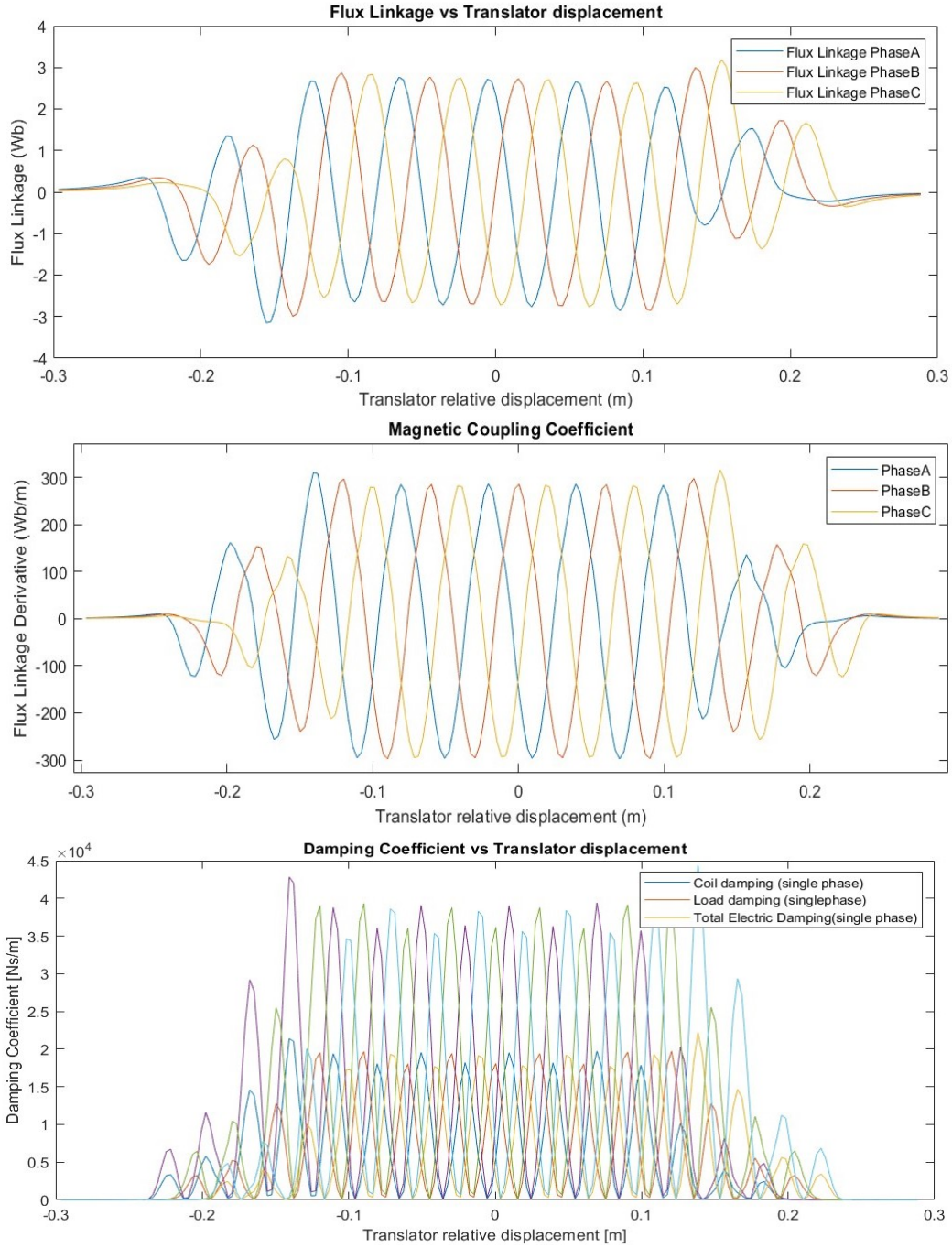

Figure 3-12: Flux linkage (ϕ_B) with respect to translator displacement (top), magnetic coupling coefficient (γ) (middle), and damping coefficients (b_T,b_C,b_L) (bottom)

3.3 Maximum power

To understand the performance of the proposed machine, it should be compared against the theoretical maximum power that could feasibly be harvested by the machine from a certain incident spectral density. Power is defined as follows:

$$P_{PTO} = F_{PTO}\dot{x}(t) = b_L\dot{x}(t)^2 \tag{3.10}$$

Assuming the incident wave load is a stationary process, and the relationship between load and response modeled as a linear, time-invariant system, the variance of the response is defined as seen in equation 3.11.

$$\dot{x}(t)^2 = \sigma_x^2 = \int_0^\infty |\,\mathbb{X}(\omega)\,|^2\, S(\omega) \tag{3.11}$$

Combining equation 2.3, 3.10, and 3.11, the average power is derived and defined as follows.

$$\begin{gathered}
\overline{P_{PTO}} = b_L \int_0^\infty S(\omega)\, |\,\mathbb{X}(\omega)\,|^2\, d\omega \\
Substitute\ in\ \mathbb{X}(\omega)\ from\ equation\ 3.4 \\
\overline{P_{PTO}} = b_L \int_0^\infty S(\omega) \frac{m^2\omega^4\, |\,\mathbb{I}(\omega)\,|^2}{m^2\omega^2 + (b_C + b_L)^2} d\omega \\
Simplify \\
\overline{P_{PTO}} = b_L \int_0^\infty S(\omega) \frac{\omega^4\, |\,\mathbb{I}(\omega)\,|^2}{\omega^2 + (\frac{2b_L}{m^2})^2} d\omega
\end{gathered} \tag{3.12}$$

By inspection of equation 3.12, the maximum theoretical power harvested is a function of the TLP RAO (assumed fixed in this study) and the incident wave spectrum, while the parameters of translator mass and the electric damping may be tuned to maximize power.

Chapter 4

WEC Control Strategy

The proposed device modeled in chapter 3 represents an idealized, passive linear harvester with unconstrained motion. This device's power harvesting potential is maximized by tuning the combined TLP and LPMG response to the peak natural frequency of the incident wave spectrum. The challenge with this strategy is that when the WEC is exposed to broadband frequencies, or an oceanic swell that shifts the peak frequency, destructive interference could lead to minimal translator motion, and in turn, low average power capture. Advancements in the vibration energy harvesting field have produced alternate strategies in effort to overcome the challenge of harvesting broadband energies and approach maximum theoretical power [30–32]. These efforts utilize techniques such as mechanical latching, shaping the potential energy well, or implementing adaptive control logic to broaden the power spectrum of the device. This chapter describes model configurations for unconstrained motion, constrained motion, and methods of implementing control strategies to the proposed LPMG design.

4.1 Unconstrained motion

To consider the ideal case of infinite stroke length, the relative motion between translator and stator, $x(t)$, is unconstrained. The electrical damping coefficient is a parameter that may be varied by adding or removing winding turns within

the constraints of the coil housing volume. The power harvested increases as the mass of the translator becomes infinite; this case is better visualized by considering a stationary translator, with the LPMG stator oscillating with TLP response to incident waves, leading to large swings in $x(t)$. Unfortunately, due to the size and material density constraints of the translator within this study, the maximum feasible translator mass is 300 kg.

The only external forces modeled for the unconstrained motion case are electrical damping and excitation force. Electrical damping, and associated power capture, only occurs when the translator is coupled with the stator between $|\,x(t)\,| < x_{coupled}$. Two unrestrained translator cases are modeled; theoretical infinite stator length with a fully coupled translator at all axial positions, giving $x_{coupled} = \infty$, and the proposed stator configuration of this study with a finite length of $x_{coupled} = 0.17$ m. For these cases, the translator equation of motion is as follows.

$$\begin{aligned} F_{inertial} + F_{PTO}[condition\ 1] &= F_{excitation} \\ F_{inertial} &= m\ddot{x}(t) \\ F_{PTO} &= \dot{x}(t)(b_C + b_L) \\ F_{excitation} &= m\ddot{\xi}(t) \\ where\ condition\ 1 &\equiv if\ \ |x(t)| < x_{coupled} \end{aligned} \tag{4.1}$$

4.2 Constrained motion

To consider the non-ideal case of limited linear space, common to all point absorbing WECs, displacement constraints must be imposed on $x(t)$ motion. For this constrained model, the trajectory limit of $|\,x(t)\,| < x_{max}$ must be implemented. To do so, equation 4.1 is altered with an additional, conditional damping force to arrest translator motion. The condition states that the force is only active at the end of translator displacement to simulate a high damping, rubber bumper that fully stops relative motion.

$$F_{inertial} + F_{PTO}[condition\ 1] + F_{bumper}[condition\ 2] = F_{excitation}$$
$$F_{bumper} = -b_{bumper}\dot{x}(t) + k_{bumper}x(t) \tag{4.2}$$
$$where\ condition\ 2 \equiv if\ |x(t)| > x_{max}$$

4.3 Latching bistable control

In the cases described thus far, translator motion is passive only, meaning the WEC is incapable of injecting energy into the system on its own, and acceleration only occurs through excitation force from incident waves. A strategy to further capitalize on this excitation force while still investigating the passive case, is to implement a logic commonly referred to as the buy-low sell-high strategy (BLSH) [31]. In accordance with this strategy, the optimal trajectory is achieved by holding the translator mass at one displacement extreme, so that $|x(t)| = x_{max}$, until the excitation force reaches a local extremum and then releasing at this peak force. Several methods have been considered to execute this latching force, including mechanical latches, electromagnets, or permanent magnets [14, 31].

The case of the mechanical latch was not considered for this study since it would require a penetration to the enclosed path of translator motion, exposing this portion of the device to air and the ocean environment. Furthermore, a mechanical contact undermines the elegance of direct energy conversion, potentially adding maintenance requirements or the risk of complete failure in the event of a faulted latch. The case of the electromagnet is advantageous with its ability to instantaneously alter the magnetic field, provide a time varying latching function, or even a repulsive force with current reversal when end magnets are fixed on the translator. Figure 4-1 displays an FEMM analysis of an iron core electromagnet designed for use in latching.

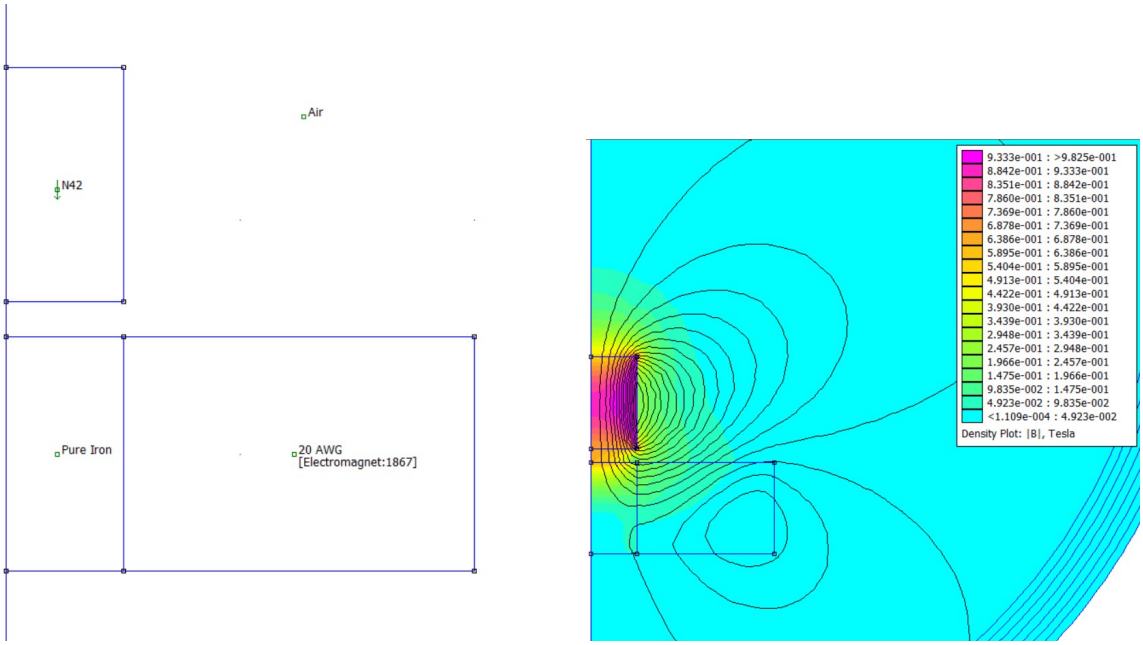

Figure 4-1: Axisymmetric FEMM analysis of an iron core electromagnet designed for LPMG control logic (stroke path oriented vertically in this image). FEMM layout is pictured left displaying an N42, translator mass end magnet, and a stationary electromagnet, with its static solution pictured right. This magnet features 1867 turns of AWG 20 wire to provide 1 Tesla with a 24V power supply.

This control electromagnet provides 50 N of latching force at 2 mm of separation between a hypothetical translator, N42, end magnet, and the iron core of the electromagnet, or -5 N when current is reversed. For the reversed current condition, the electromagnetic repelling force is offset by the iron core attracting the permanent magnet.

Unfortunately, early design iteration and analysis identified that coil resistance power dissipation outweighed the benefits of this control system. Therefore, a similar strength permanent magnet is considered, oriented with attracting poles in the latch condition, and rotated 90 degrees to implement the desired unlatching condition. To permit rotation, the minimum distance between magnets is 2mm, where latching force is 100 N and unlatching force is 0 N. Figure 4-2 displays this arrangement for the negative x_{max} position.

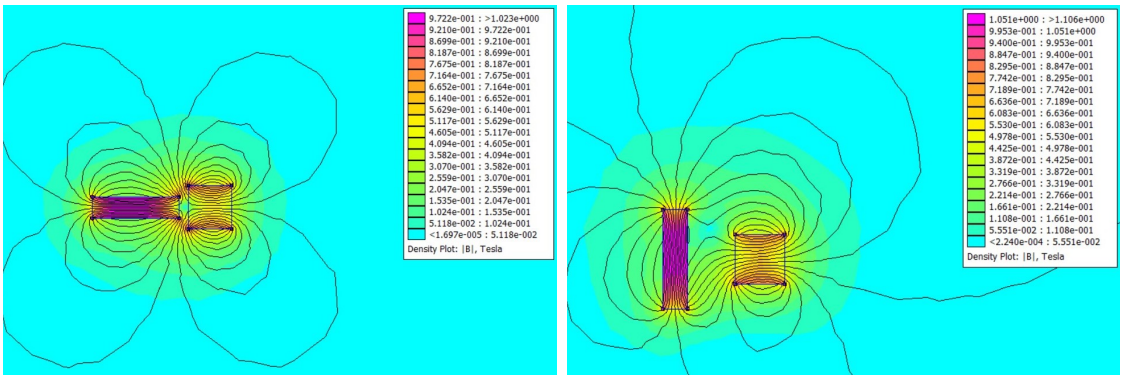

Figure 4-2: Planar FEMM solution of a long rectangular, N42, rotating magnet for use in LPMG control logic, the square N42 magnet in the images is mounted on the left end of the translator. The left image displays the latched position, while the right image displays the unlatched position.

As previously stated, the control logic states that at peak excitation force, the latch must be released. This peak excitation occurs when $\ddot{\xi}(t) = Local\ Extreme$, or alternatively stated, $\dddot{\xi}(t) = 0$. This logic implemented in closed form is seen in equation 4.3. To avoid spurious rotations, the condition is implemented only when $|x(t)| > \frac{x_{max}}{2}$.

$$F_{inertial} + F_{PTO}[cond.\ 1] + F_{bumper}[cond.\ 2] + F_{latch}[cond.\ 3] = F_{excitation}$$

$$\begin{aligned} where\ condition\ 3 \equiv \quad & if\ x(t) < \frac{-x_{max}}{2} \ \ \& \ \ \dddot{\xi}(t) < 0 \\ & or\ x(t) > \frac{x_{max}}{2} \ \ \& \ \ \dddot{\xi}(t) > 0 \\ & then\ F_{latch} = Latch\ Func.\ (figure\ 4-3) \\ & else\ F_{latch} = 0 \end{aligned} \tag{4.3}$$

The latching condition described in figure 4-3 creates a force profile with two potential energy "wells", where the translator mass finds stability from the latching end magnet holding the translator against the stroke end-stop bumper. A device with this condition is referred to as having a bistable potential [31].

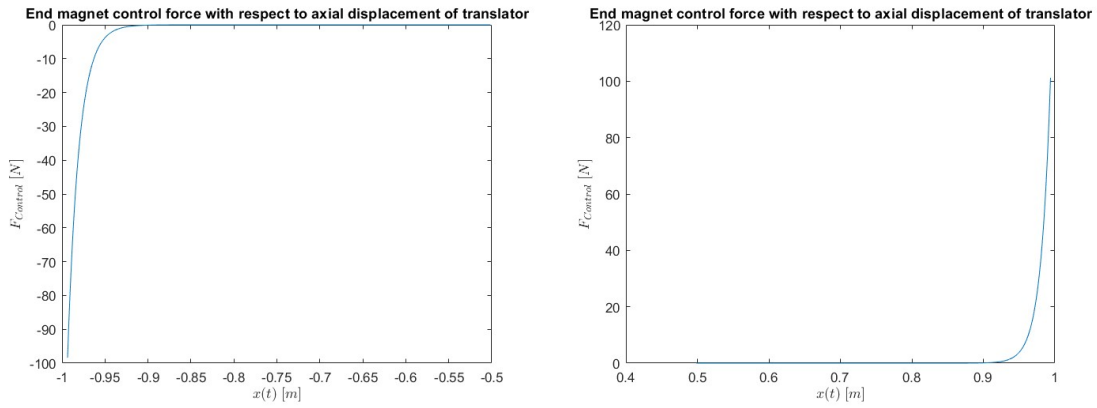

Figure 4-3: Latching control force vs translator mass axial displacement while in the latched condition for both the $-x_{max}$ position (left image) and x_{max} position (right image).

4.4 Adaptive bistable control

To expand upon the concept of bistable latching control, the forcing function may be altered such that in the unlatched condition, the control force is reversed. This is achieved by rotating the end magnet 180 degrees to align like poles, resulting in a repelling force as described in equation 4.4.

$$F_{inertial} + F_{PTO}[cond.\ 1] + F_{bumper}[cond.\ 2] + F_{control}[cond.\ 4] = F_{excitation}$$

$$\begin{aligned} & & if\ x(t) < \frac{-x_{max}}{2} \ \ \& \ \ \dddot{\xi}(t) < 0 \\ where\ condition\ 3 \equiv & & or\ x(t) > \frac{x_{max}}{2} \ \ \& \ \ \dddot{\xi}(t) > 0 \\ & then\ F_{latch} = Latching\ Function\ (figure\ 4-3) & \\ & else\ F_{latch} = Unlatching\ Function\ (figure\ 4-4) & \end{aligned} \tag{4.4}$$

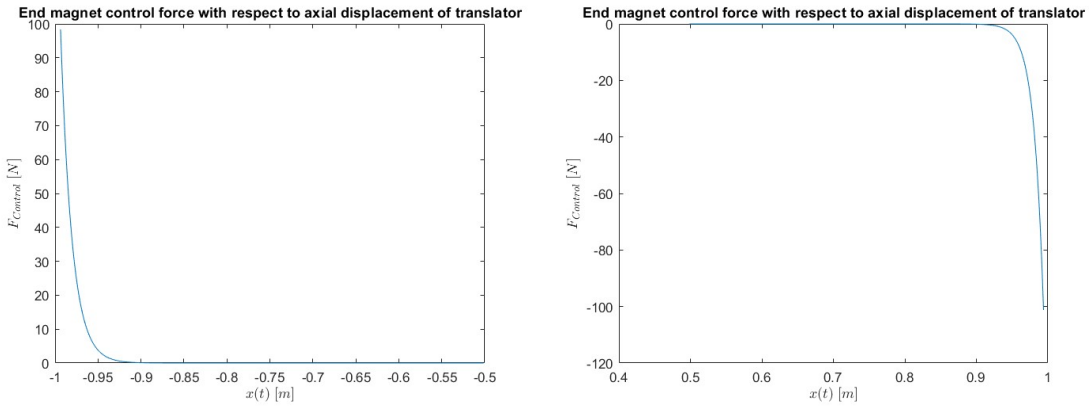

Figure 4-4: Unlatching control force vs translator mass axial displacement while in the unlatched condition for both the $-x_{max}$ position (left image) and x_{max} position (right image).

The adaptive control logic described creates two bistable potential wells that can be implemented conditionally. As proposed in this study, the challenge with creating two bistables is that rotation of the control end-magnets will come at an energy cost that detracts from the total energy harvested. To quantify this energy loss, the torque experienced was measured at each angular increment during rotation. This measurement was performed in FEMM, and results are plotted in figure 4-5. The total work required to overcome each rotation is determined to be 2.0 J, and can be seen calculated in equation 4.5.

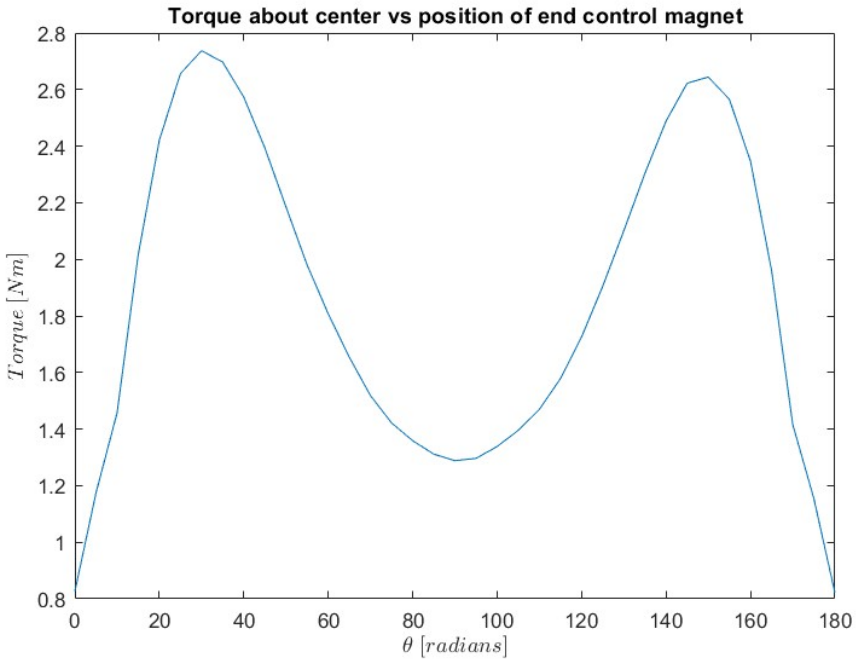

Figure 4-5: Torque about center vs angular position for the end control magnet.

$$Work = \int \tau d\theta = 5.9\, J \tag{4.5}$$

Chapter 5

Analysis and Results

This chapter outlines the numerical modeling method used to predict the performance of scenarios introduced within chapter 4, along with discussion and recommendations.

5.1 Method of analysis

To solve the translator equation of motion while implementing the conditional statement imposed by translator-stator coupling, or translator displacement constraints, the equation must be solved as an Ordinary Differential Equation (ODE) in the time domain. This ODE is solved via MATLAB computing platform by implementing a Runge-Kutta method with variable time steps. The simulated time history TLP response motion, discussed in section 3.1.3, contributes to the excitation force within the ODE; the format of this simulated signal is a data array that must be converted to a function for use in the MATLAB ODE solver. Fitting a random, broadband signal is non-trivial, thus a 150-term Fourier series function is used to convert each of the TLP simulated response trials, to a time dependent function. Examples of this fit function are provided in figure 5-1.

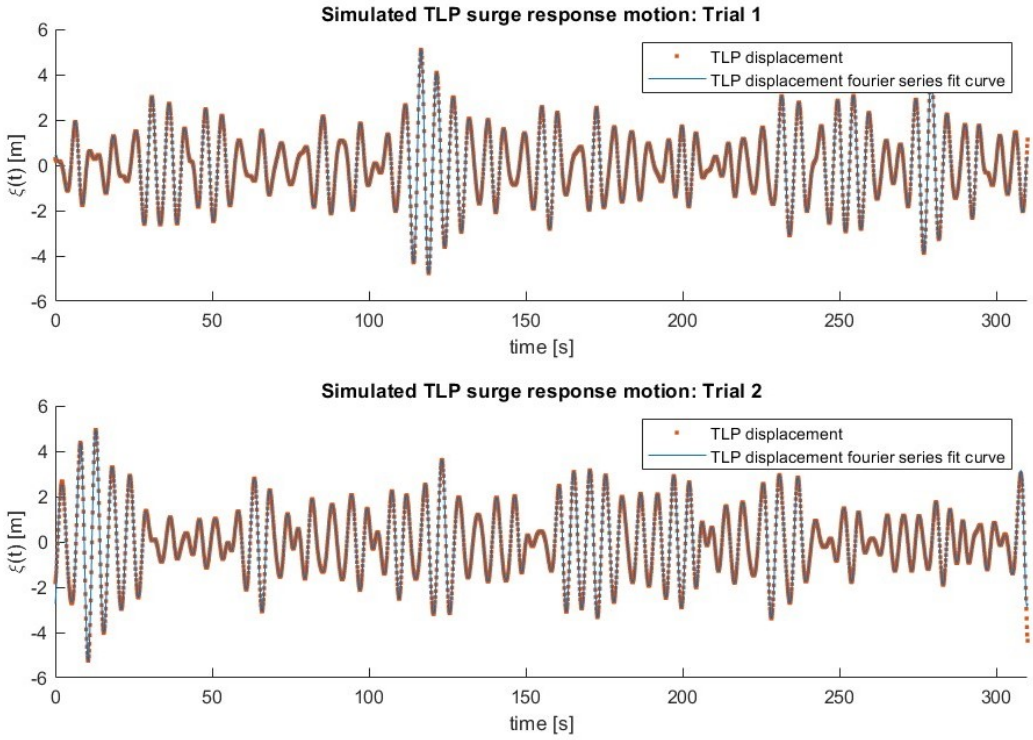

Figure 5-1: TLP simulated displacement data plotted along with a 150-term Fourier series fit curve for trials 1 (top) and 2 (bottom).

The time history wave elevation signals were randomly generated as discussed in section 2.2.1, which in turn will produce a unique and random TLP response signal. Therefore, ten trials were performed to produce TLP response signals; these ten trials are used to calculate each case to ensure repeatability of results and accuracy of predicted performance. The first two trials are displayed in figure 5-1.

5.2 Unconstrained motion

Unconstrained translator motion, with a theoretical infinite stator length, is the first case considered. Results matched predictions, revealing that the maximum feasible power harvested rises as translator mass is increased. For the hypothetical infinitely large translator mass, a point of diminishing return exists for every value of total EMF damping coefficient, b_T ($where\ b_T = b_C + b_L$), this is illustrated in figure 5-2

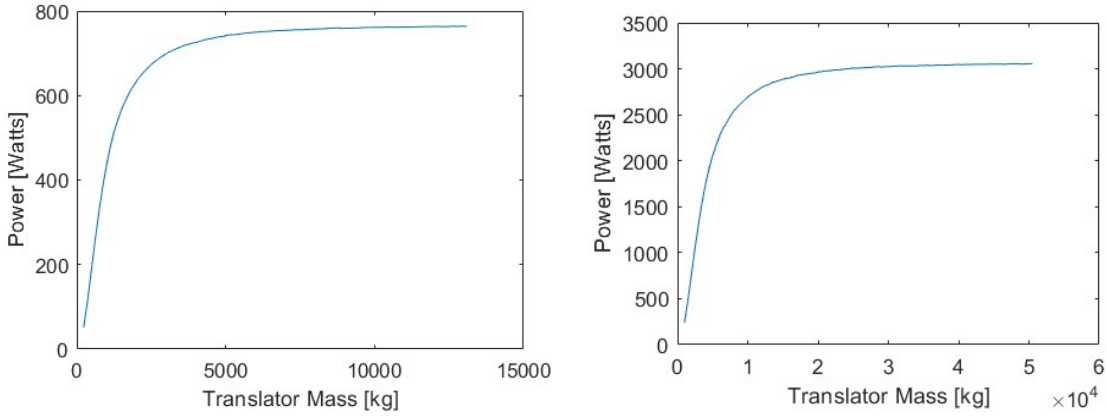

Figure 5-2: Theoretical power harvested from a fully coupled, infinite stroke length LPMG, during a 310-second simulation (trial 1) with increasing translator mass for a b_T of 1000 Ns/m (left image) and 4000 Ns/m (right image).

Figure 5-2 right hand image shows the case of a 4000 Ns/m damping coefficient; this value represents the maximum achievable value for a fully coupled LPMG with infinite stroke and stator length. Although 3 KW could theoretically be harvested with this damping coefficient, it is apparent that the proposed design is severely limited in the ability to increase translator mass. Therefore, a tunable damping coefficient is desired to accommodate the lower translator mass values considered in this study, and can easily be achieved by altering winding turns. Alternatively, future design iterations could achieve this reduction through weaker permanent magnets, or by increasing the flux air gap, both solutions are cost saving measures, with the latter allowing for more relaxed manufacturing tolerances.

When considering specific values of translator mass, there exists an optimal damping coefficient for each discrete value of translator mass. This relationship is portrayed in figure 5-3.

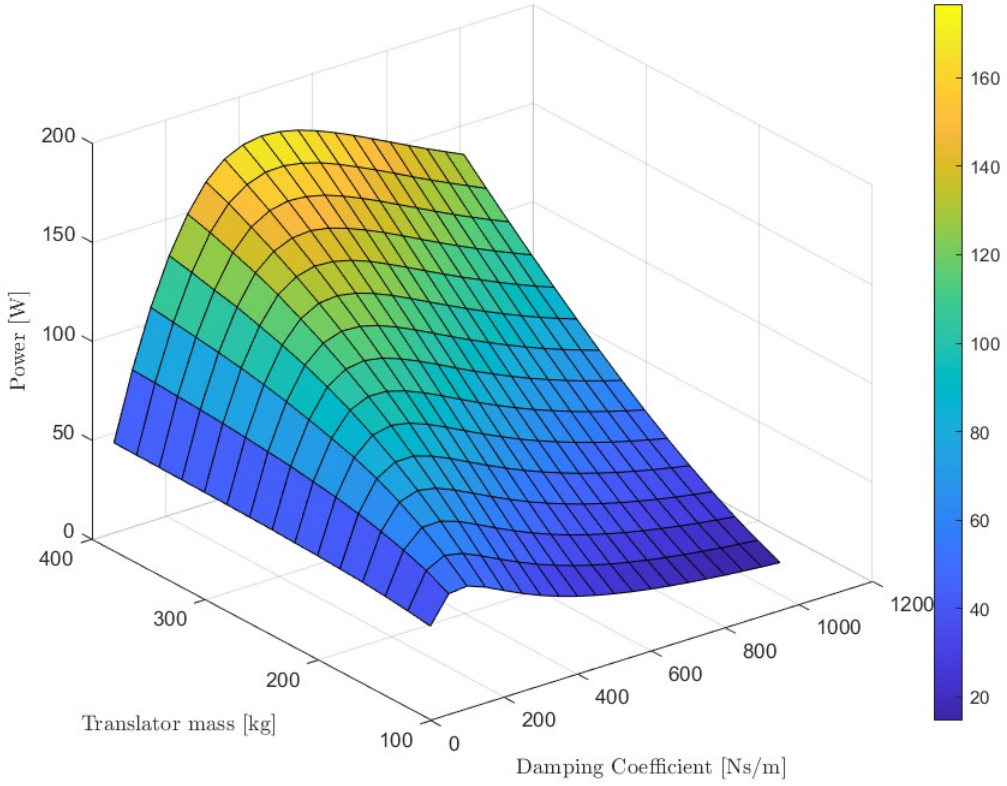

Figure 5-3: Heat map of power harvested during a 310-second simulation (trial 1), with varying b_T and translator mass. The peak power of this 3D plot represents the optimal damping coefficient and translator mass combinations for the fully coupled case.

For the infinite stroke and stator length, with a maximum achievable translator mass of 300 kg, the optimal damping coefficient occurs at 350 Ns/m. The resulting power capture for this case is 133 W, with a standard deviation of 0.04 W for the ten trials. Results of Trial 1 are displayed in figure 5-4. It is noted that the maximum displacement only reaches a value of 2.5m, suggesting that an LPMG with a 5m stroke length is sufficient for this design case; the TLP design could easily house a platform to accommodate this length.

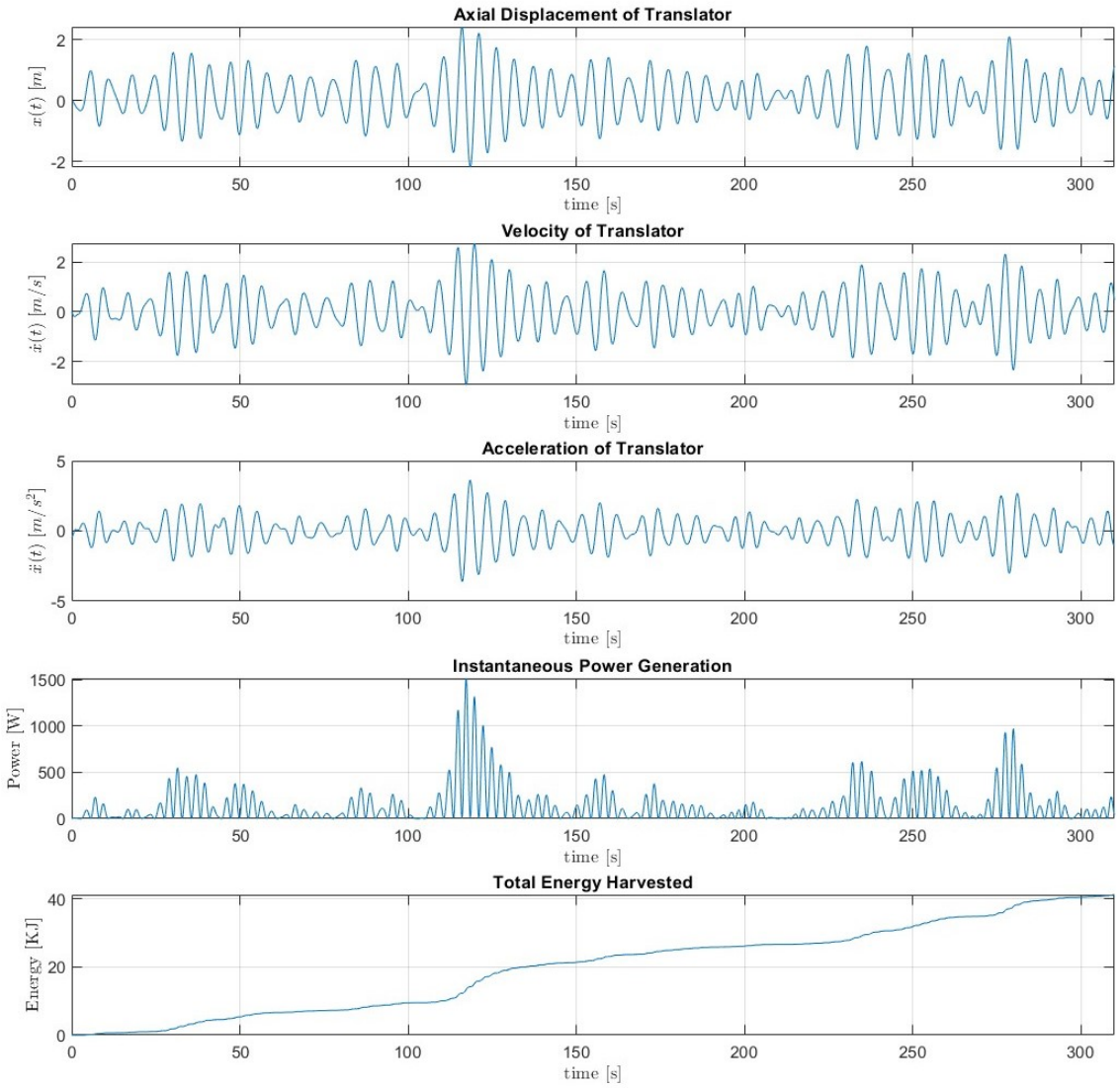

Figure 5-4: Trial 1 simulation for a fully coupled, infinite stroke length with $b_T = 350$ Ns/m and translator mass of 300 kg. Max power capture for this trial is 132.6 W.

The second case considers infinite stroke length while implementing a finite stator length. Unfortunately, during all trials, the unbalanced force injected into the system by the EMF damping caused the translator mass to drift away from the center position of $|\,x(t)\,| < x_{coupled}$, where coupling and the associated energy harvesting occurs. For this reason, the infinite stroke length with finite stator case is revised to a constrained case with a long stroke length, and will be discussed in the following section.

5.3 Constrained motion

To simulate an infinitely long stroke length, while ensuring the translator mass does not drift far from the harvesting region, a semi-infinite stroke length of 6 m is selected ($x_{max} = 3$ m), with $x_{coupled} = 0.17$ m, while the bumper force and conditions discussed in equation 4.2 are implemented. A sensitivity analysis revealed that the optimal damping coefficient for this case is $b_T = 3600$ Ns/m, as portrayed in figure 5-5.

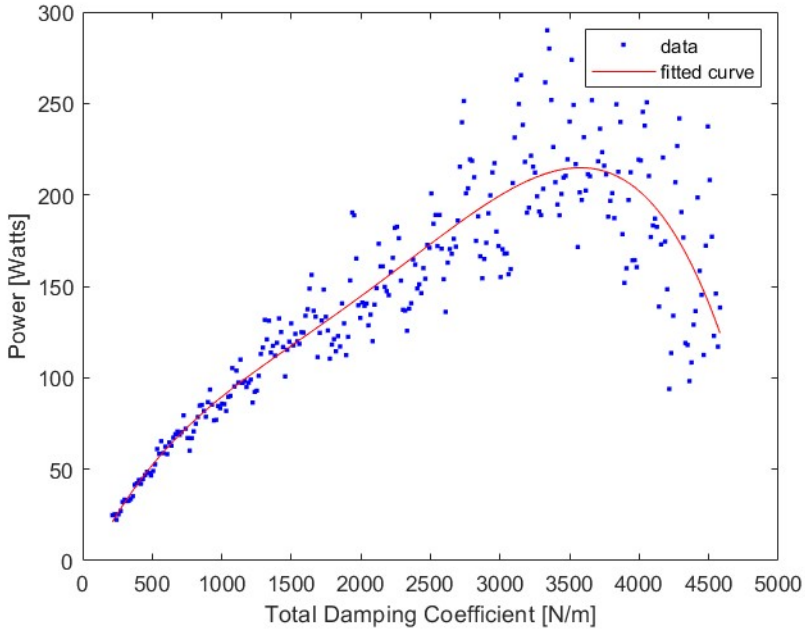

Figure 5-5: Power harvested during a 310-second simulation (trial 1), with varying b_T for $x_{max} = 3$ m, $x_{coupled} = 0.17$ m, and a translator mass of 300 kg.

Although the trend is observable, it can be seen that widely varying results are produced, even with slight changes in damping coefficient. This occurs as the translator mass becomes "trapped" with low velocity in the highly damped harvesting region for various lengths of time. Although low power is harvested during these trapped periods, once the mass is freed due to a large enough acceleration, the high velocities achieved during the long stroke lead to high instantaneous power capture. As indicated by the fitted curve, the resulting power capture predicted for this case is 210 W, with a standard deviation of 14 W for the ten trials. The predicted

power capture is 58% higher than the fully coupled case, suggesting that allowing the translator mass to achieve higher speeds by not damping the ends of stroke length greatly improves results, even if periods of low capture must be endured. An additional benefit of this design configuration is that a shorter stator length will reduce overall LPMG costs. Figure 5-6 displays a trial run of this case; the axial displacement of translator plot aids in showing periods where the translator mass remains trapped in the harvesting region.

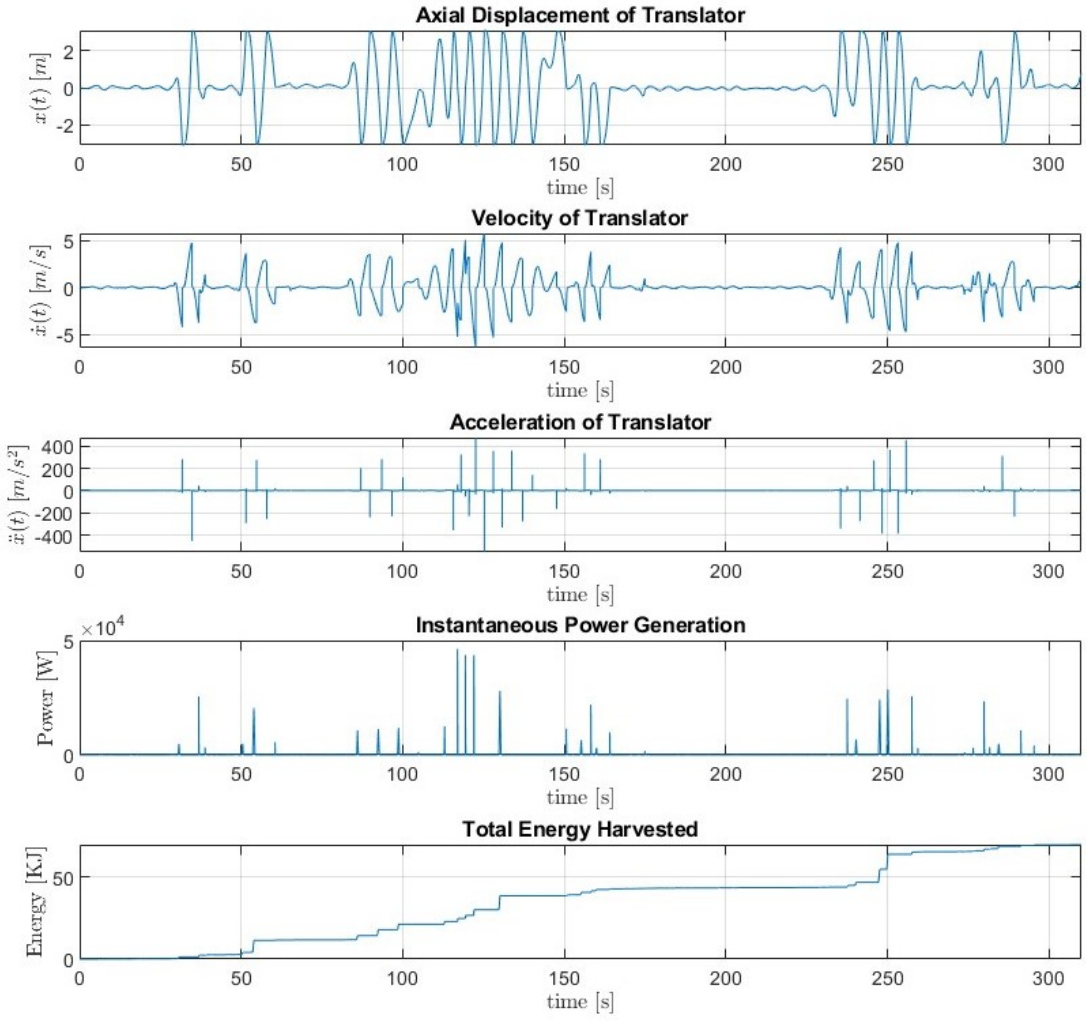

Figure 5-6: Trial 2 simulation for $x_{max} = 3$ m, $x_{coupled} = 0.17$ m, $b_T = 3600$ Ns/m, and a translator mass of 300 kg. Max power capture for this trial is 224.4 W.

The second constrained motion case investigated considers a shortened stator length to explore the effect on power density, and further reduce manufacturing costs. This configuration features a stroke length of 2 m ($x_{max} = 1$ m), with $x_{coupled} = 0.17$ m, while the bumper force and conditions discussed in equation 4.2 remain in place. This design configuration also represents the case selected for further control theory implementation that will be discussed in the following sections.

As indicated by the fitted curve in figure 5-7, the resulting power capture predicted for this case is 95 W, with a standard deviation of 12 W for the ten trials. Figure 5-8 displays an example trial of this configuration. The optimal damping for this reduced stroke length case is $b_T = 2100$ Ns/m.

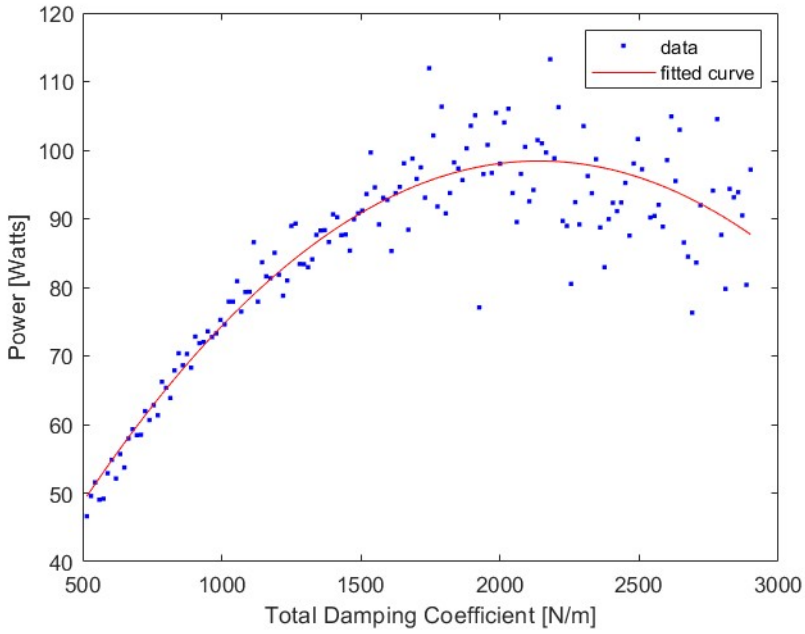

Figure 5-7: Power harvested during a 310-second simulation (trial 1), with varying b_T for $x_{max} = 1$ m, $x_{coupled} = 0.17$ m, and a translator mass of 300 kg.

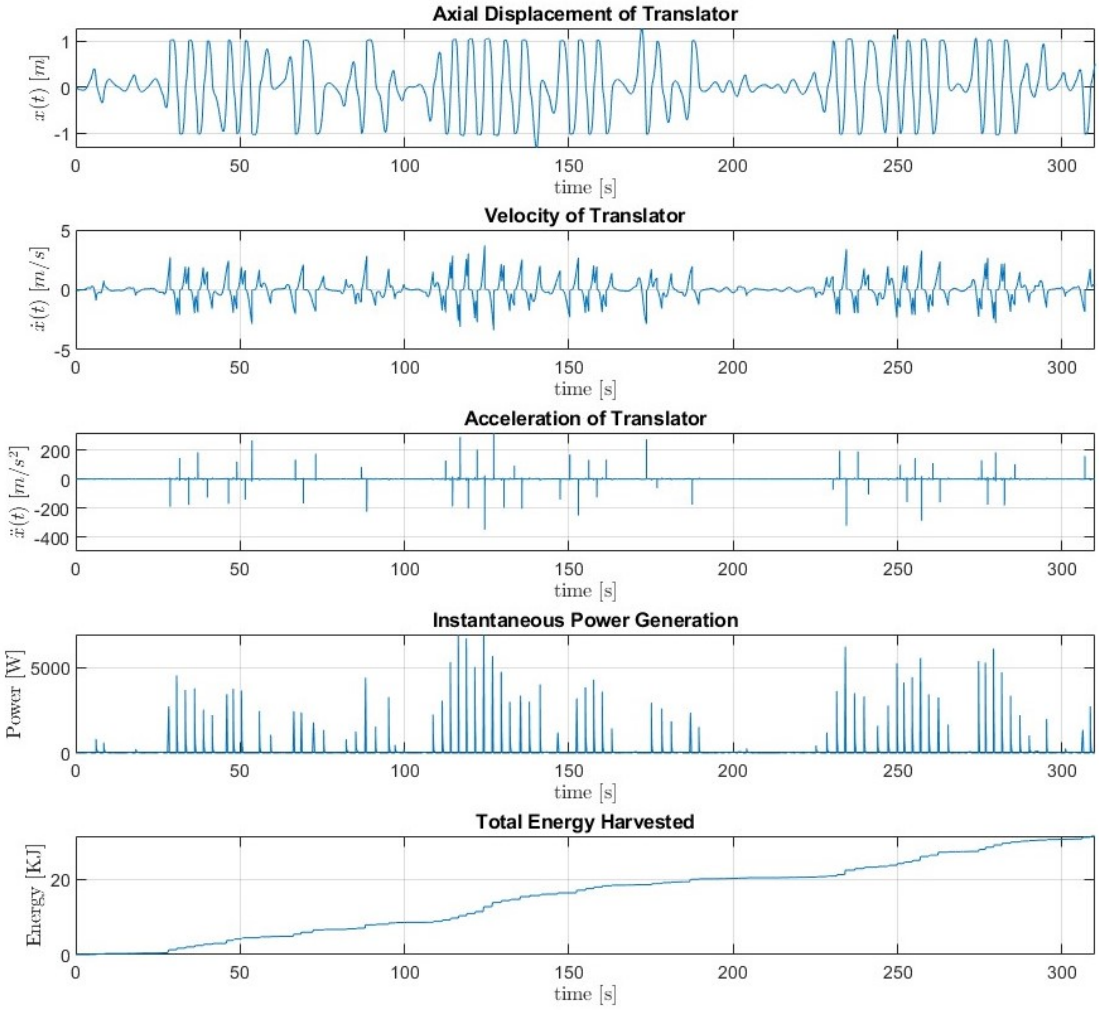

Figure 5-8: Trial 2 simulation for $x_{max} = 1$ m, $x_{coupled} = 0.17$ m, $b_T = 2100$ Ns/m, and a translator mass of 300 kg. Max power capture for this trial is 105.1 W.

With an additional volume factor added for mounting, the estimated volume of this LPMG is reduced from 3.6 m^3 for the 6 m stroke length, to 1.4 m^3 for the 2 m stroke length. This represents a 61% reduction in volume, which is similar to the 57% reduction in predicted power capture (from 224 to 95 w for the 6 and 2 m stroke lengths, respectively). This indicates that either stroke length investigated would result in a similar power density of 62 W/m^3 for a 6 m stroke length and 68 W/m^3 for a 2 m stroke length.

These results open the discussion for a stroke length sensitivity analysis. However, it is emphasized that this study is only applicable to the sea state and spectrum

selected. Stroke length was varied from 1 m to 12 m in 0.25 m step increments, and a power vs damping parametric study was performed at each step (as was performed in figure 5-5). The peak power, as indicated by the fitted curve for each parametric study, and the respective power density were then plotted against x_{max}, results are displayed in figure 5-9. The maximum power harvested of 210 W occurs at the 6 m stroke length (x_{max} = 3 m), while maximum power density occurs at 2.5 m stroke length (x_{max} = 1.25 m) of 70 W/m^3.

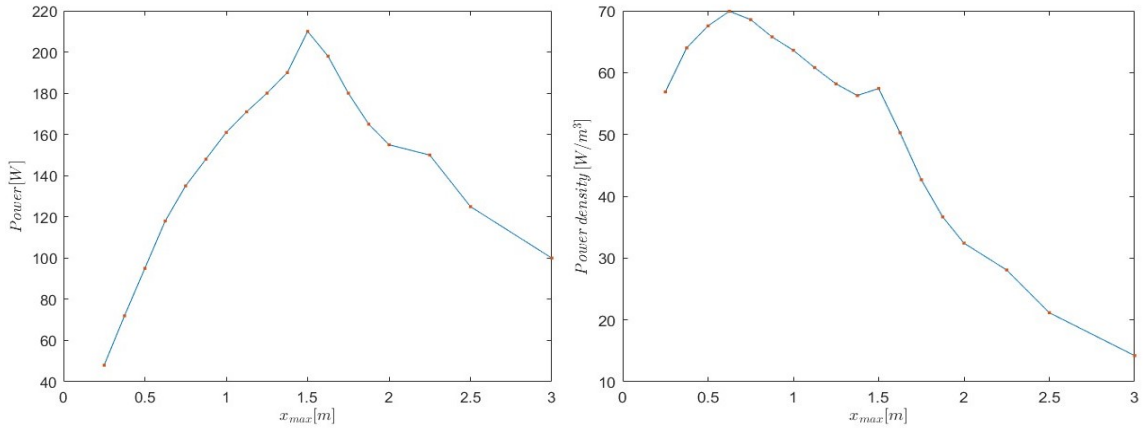

Figure 5-9: Sensitivity analysis of stroke length vs predicted power capture (left) and power density (right).

5.4 Latching bistable control

The latching control case considers a stroke length of 2 m (x_{max} = 1 m), with $x_{coupled}$ = 0.17 m, while the bumper force and conditions discussed in equation 4.2 remain in place, and the additional magnetic latching logic from equation 4.3 is implemented. Over the ten trials performed, the latching control parametric study revealed almost no advantage over the case with no latch, with respect to power

capture and standard deviation of results. Only a 1.2 percent higher predicted power harvesting was realized, with optimal damping occurring at 2140 Ns/m. However, the latching control led the LPMG to harvest energy through a very different path. Figure 5-10 displays the same trial with and without latching control; in the axial displacement plot, notice the effectiveness of the magnetic latch to hold the translator mass at x_{max}, and then release at the strategic time. This logic clearly increases peak velocity, which in turn increases short periods of instantaneous power capture.

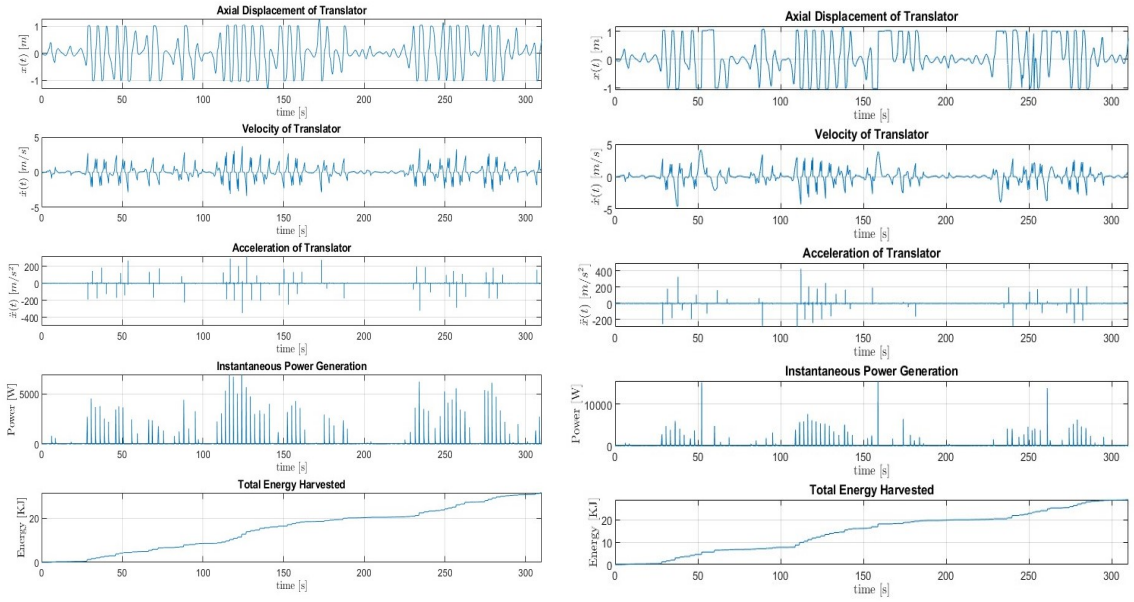

Figure 5-10: Trial 2 simulation for $x_{max} = 1$ m, $x_{coupled} = 0.17$ m, $b_T = 2100$ Ns/m, and a translator mass of 300 kg. Power capture is equivalent for both simulations, left image shows no latching, while right image implements latching control logic.

With comparable power capture between the case of latching control logic and no latching, implementation of latching control is not recommended. The higher instantaneous power generation will result in high amperage that could lead to undesirable resistive power losses and associated heat generation within the stator.

5.5 Adaptive bistable control

The adaptive bistable control case considers the same conditions as the latching scenario, but with the additional unlatching forcing function incorporated, as described in equation 4.4. The resulting power capture predicted for this scenario provided 101 W, as indicated by the fitted curve in figure 5-11, with a standard deviation of 12 W for the ten trials. Figure 5-12 displays an example trial of this configuration. The optimal damping for this LPMG configuration and control logic is $b_T = 2200$ Ns/m.

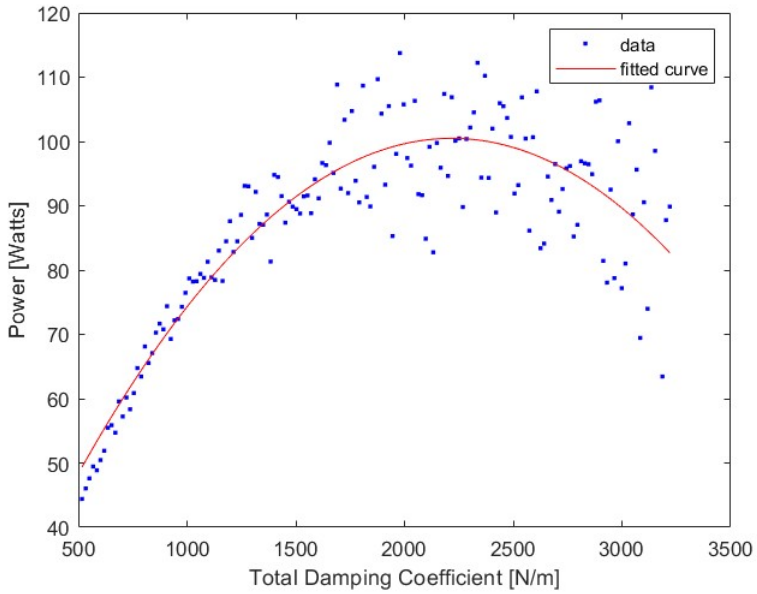

Figure 5-11: Power harvested during a 310-second simulation (trial 1), with adaptive bistable control and varying b_T for $x_{max} = 1$ m, $x_{coupled} = 0.17$ m, and a translator mass of 300 kg.

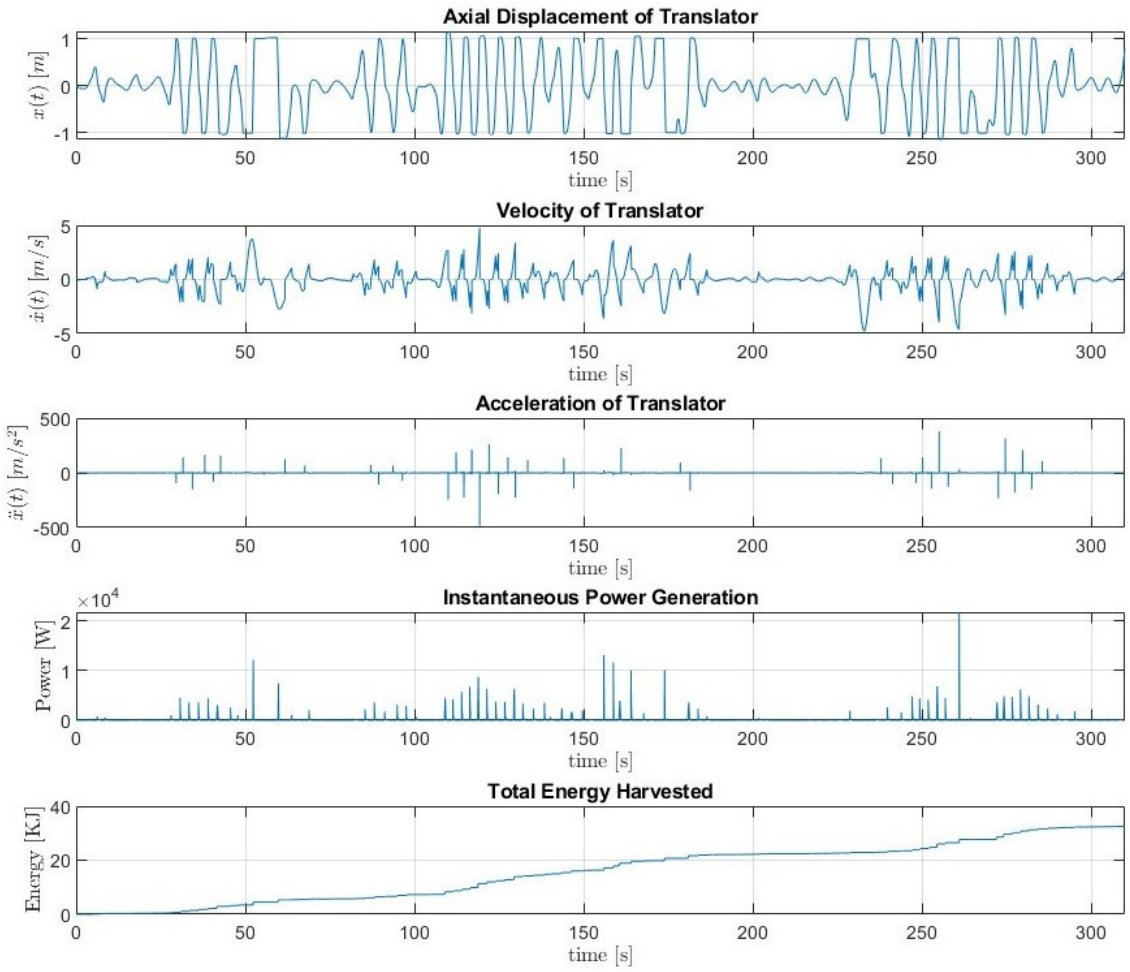

Figure 5-12: Power harvested during a 310-second simulation (trial 1), with adaptive bistable control and $b_T = 2100$ Ns/m for $x_{max} = 1$ m, $x_{coupled} = 0.17$ m, and a translator mass of 300 kg.

This design configuration realizes a promising 6.3% higher power capture than the passive case with the same stroke length and stator-translator configuration. However, the power required to operate the control magnets must be determined to reveal the net power capture. Considering both end control magnets, between 50-70 rotations occurred during each of the ten trials. Using the most conservative value of 70 rotations, and the 5.9 J/rotation determined in equation 4.5, approximately 413 J are required during the trial period in order to implement adaptive bistable control logic. This translates to the loss of 1.3 W, still leading to the adaptive bistable control

case contributing a 4.9% net power improvement over the case with no control. The revised 100 W device would have a power density of 72 W/m^3, or if considering the footprint alone, 96 W/m^2 for the LPMG.

Chapter 6

Conclusion and Future Work

This study investigated the promising future of renewable energy by proposing a theoretical WEC in the form of a TLP featuring an LPMG for direct energy conversion. The LPMG is oriented horizontally in effort to harvest energy in the surge displacement of the TLP. Modeling and simulations revealed that stroke length, electric damping, and mass of the translator are parameters that can be varied to optimize performance of the device, and that implementing active bistable control can result in higher net energy capture.

6.1 Conclusion

The first parameters investigated for the LPMG considered were electrical damping and translator mass. A sensitivity analysis revealed that as mass increases, power harvested will increase. However, for each mass value selected, there exists an optimal damping that is dependent on the LPMG configuration. For this reason, careful design of the stator-translator is important to ensure that magnetic coupling leads to this optimal damping.

Early design configurations investigated in this study featured an LPMG with a fully coupled stator-translator, as well as the case of an LPMG with a short stator located in the center of translator stroke length. Simulations revealed that, although harvesting power for much less time, the short stator improved the overall power

harvested. Not damping the end of the stroke length allows for the translator to accelerate to higher velocities prior to entering the harvesting reason, with power directly proportional to translator velocity this leads to higher instantaneous power generation that will lead to a higher average power capture. Specifically, a fully coupled LPMG with infinite stroke length, and optimal damping of 350 Ns/m, will result in average power of 133 W, while the translator stroke rarely exceeded 4 m. When compared to the case of a short, finite stator with 0.24 m of magnetic coupling length, while the translator was permitted to freely oscillate along a 6 m stroke length, the machine averaged 210 w; a 58% increase.

A stroke length sensitivity analysis was performed for an LPMG with a short stator-translator coupled region, and the optimal stroke length for high power capture was 210 W at 6 m long, while the highest power density occurs at a 2.5 m stroke length, with 70 W/m^3 (or a footprint of 93 W/m^2).

Using an LPMG configuration with a 2 m stroke length and a finite stator for comparison, two control cases were investigated that implement BLSH logic by actuating a control end-magnet at peak excitation force; latching control and adaptive bistable control. The latching control case resulted in negligible improvement over the passive case and resulted in undesirably high instantaneous power capture, thus is not recommended for consideration. However, the adaptive bistable control resulted in a net 4.9% improvement over the passive case. Implementation of this control logic is recommended, but consideration must be taken to mitigate the concerns that may arise due to the higher instantaneous power capture that was observed during this study.

6.2 Future work

Overall, this study revealed that by tuning the parameters of stroke length, electrical damping, and length of the magnetically coupled region, while implementing an adaptive bistable control logic, an improved LPMG design configuration can be produced for a certain incident wave spectrum and TLP layout. Selection of these values can lead to higher power capture for an individual LPMG, or produce higher

machine power density; ultimately, preference of this outcome relies on how multiple LPMGs are arranged on a TLP, or could be a function of wave farm layout incorporating multiple TLPs. As a result, no one specific recommendation can be made for LPMG design until the TLP or wave farm arrangement is decided. This decision is outside the scope of this study, and thus will be left as an area of future work.

Incorporation of adaptive bistable control logic reveals several considerations that should be included in future studies. First, the higher instantaneous power generation that results from this control logic could lead to higher resistive power loss and associated heat generation. This effect on net power capture should be quantified, and methods of mitigating this concern should be investigated, such as lower winding resistance or methods of heat dissipation. Secondly, the adaptive bistable control assumption relied on past studies that suggest actuation of control end-magnets should occur at peak excitation force [30]. However, the optimal actuation point for the BLSH logic could occur slightly before this value, therefore, the optimal actuation point should be investigated. If an earlier actuation point is found preferable, the calculation of peak excitation force can no longer be determined instantaneously and a method of forecasting would be necessary. Finally, due to the complexity of designing, modeling, and analyzing a control end-magnet in FEMM, only one end-magnet design case was considered and was based on the expected peak force for the selected spectrum and translator mass. A quick simulation was performed and revealed that if the adaptive bistable control forcing function is increased by three times the value (peak magnetic force of 300 N vice 100 N), the gross power improvement over the passive case increases to 21 percent, compared to the present 6.3 percent. The rotational torque to overcome this stronger magnet was not calculated or considered, but is expected to be much less than the realized gains. For this reason, it is recommended that the preferred control force be further investigated.

In this study, only one finite stator length was considered. It is likely that a parametric study of the coupled stator-translator length vs stroke length could further improve LPMG performance and should be considered in future work. When considering stroke length variation, we are effectively tuning the device to promote

resonance when considering a specific incident sea state spectrum. If the incident spectrum drastically changes, which occurs often in the ocean environment due to storms or seasonality, the optimal stroke length will likely change. For this reason, it is recommended that the stroke length sensitivity analysis performed in section 5.3 be conducted for various sea states. The results of this study are likely to lead to a wide range of recommended values. This, in turn, could result in an additional aspect of LPMG control, namely, adaptive stroke length through movable end stops.

The 300 kg translator repetitively slamming into end stops during routine operation could potentially lead to longevity concerns. For this reason, the mounting system for the LPMG should be designed in detail. Additionally, a method of arresting translator motion while minimizing impact loads should be investigated, such as improved end-stop damping or the inclusion of end springs.

Finally, this study assumed that the TLP tendon pretension could be set in such a manner that C_{11}^{E} produces maximum surge compliance for the TLP response. A detailed engineering analysis should be performed for this external restoring coefficient to determine not only if the constant value assumed in this study is feasible, but if a non-linear restoring coefficient could be produced by the tendons such that equation 3.2 considers a range of $A_{11}(\omega)$ based on incident frequency, rather than the discrete value selected for A_{11}^{*}.

Appendix A

FEMM Lua Script

This script generates an FEMM mesh, solves the magnetostatic problem, then moves axial position of translator by 3mm, records data, and repeats for 180 iterations. The data recorded includes flux linkage for each of three phases and axial force, written to four separate CSV files.

$mi\_createmesh()$
$handleA = openfile('C:locationoffile\PhaseA.csv','w')$
$handleB = openfile('C:locationoffile\PhaseB.csv','w')$
$handleC = openfile('C:locationoffile\PhaseA.csv','w')$
$handleD = openfile('C:locationoffile\Force.csv','w')$
$for\, i = 180, 1, -1$
do
$mi\_analyze(0)$
$mi\_loadsolution()$
$write(handleA, mo\_getcircuitproperties("PhaseA"))$
$write(handleA, "\n")$
$write(handleB, mo\_getcircuitproperties("PhaseB"))$
$write(handleB, "\n")$
$write(handleC, mo\_getcircuitproperties("PhaseC"))$
$write(handleC, "\n")$

$mo\_groupselectblock(1)$

$write(handleD, mo\_blockintegral(19))$

$write(handleD, "\backslash n")$

$mi\_seteditmode("group")$

$mi\_selectgroup(1)$

$mi\_movetranslate(y, 3)$

end

$closefile(handleA)$

$closefile(handleB)$

$closefile(handleC)$

$closefile(handleD)$

Bibliography

[1] Andrew Cornett. A Global Wave Energy Resource Assessment. In *Proceedings of the eighteenth international offshore and polar conference*, volume 50, 11 2008.

[2] Budi Azhari, Fransisco Danang Wijaya, and Edwar Yazid. Performance of Linear Generator Designs for Direct Drive Wave Energy Converter under Unidirectional Long-Crested Random Waves. *Energies*, 14(16), 2021.

[3] Abdus Samad, S. A. Sannasiraj, V. Sundar, and Paresh Halder. *Ocean wave energy systems: Hydrodynamics, power takeoff and control systems*. Springer Nature, Cham, Switzerland, 8 2021.

[4] D. L. Bruschi, J.C.S. Fernandes, A.F.O. Falcão, and C.P. Bergmann. Analysis of the degradation in the wells turbine blades of the pico oscillating-water-column wave energy plant. *Renewable and Sustainable Energy Reviews*, 115:109368, 11 2019.

[5] Simon P. Neill and M. Reza Hashemi. *Fundamentals of ocean renewable energy: Generating electricity from the sea*. Elsevier Ltd., 2018.

[6] David F. H. Larson. *Quasi-Monte Carlo and Picard Iteration Algorithms for the Nonlinear Hydrodynamics, Dynamics and Controls of Wave Energy Converters*. PhD dissertation, Massachusetts Institute of Technology, Department of Mechanical Engineering, 2021.

[7] Zhiwei Zhang, Bocheng Wu, Qinfen Lu, and Wei Xu. Novel linear generator concepts and topologies for wave energy conversion systems: A review. *2021 13th International Symposium on Linear Drives for Industry Applications (LDIA)*, pages 1–6, 2021.

[8] Jing Zhang, Haitao Yu, Qi Chen, Minqiang Hu, Lei Huang, and Qiang Liu. Design and experimental analysis of ac linear generator with halbach pm arrays for direct-drive wave energy conversion. *IEEE Transactions on Applied Superconductivity*, 24:1–4, 2014.

[9] Jiabin Wang and D. Howe. Design optimization of radially magnetized, iron-cored, tubular permanent-magnet machines and drive systems. *IEEE Transactions on Magnetics*, 40:3262–3277, 2004.

[10] Naveen Kumar Arora and Isha Mishra. COP26: more challenges than achievements. *Environmental Sustainability*, 4(4):585–588, 2021.

[11] Lorenz Moosmann. *The COP27 climate change conference.* European Parliament, 2022.

[12] Johannes Falnes. *Ocean waves and oscillating systems.* Cambridge University Press, Cambridge, England, 1 2005.

[13] Reza Jafari, Pedram Asef, Mohammad Ardebili, and Mohammad Mahdi Derakhshani. Linear Permanent Magnet Vernier Generators for Wave Energy Applications: Analysis, Challenges, and Opportunities. *Sustainability*, 2022.

[14] Joao Cruz. *Ocean Wave Energy: Current status and future perspectives, Green Energy and Technology.* Springer Berlin, Heidelberg, 2008.

[15] Omar Farrok, Koushik Ahmed, Abdirazak Dahir Tahlil, Mohamud Mohamed Farah, Mahbubur Rahman Kiran, and Md. Rabiul Islam. Electrical Power Generation from the Oceanic Wave for Sustainable Advancement in Renewable Energy Technologies. *Sustainability*, 12(6), 2020.

[16] M. Prado and H. Polinder. Case study of the Archimedes Wave Swing (AWS) direct drive wave energy pilot plant. In *Electrical Drives for Direct Drive Renewable Energy Systems*, pages 195–218. Woodhead Publishing, 2013.

[17] M. K. Ochi. *Ocean waves: the stochastic approach.* Elsevier Ltd., 1998.

[18] S.K. Chakrabarti. *Handbook of Offshore Engineering*, volume I. Elsevier Ltd., 2005.

[19] Lionel I. Moskowitz and Willard J. Pierson. *Wave spectra estimated from wave records obtained by the OWS Weather Explorer and the OWS Weather Reporter.* New York University, College of Engineering, Research Division, Dept. of Meteorology and Oceanography, 1962.

[20] C.-H. Lee. *WAMIT Theory Manual*, 1995.

[21] Liang Yan, Lu Zhang, Peng Juanjuan, Lei Zhang, and Jiao Zongxia. *Electromagnetic Linear Machines with Dual Halbach Array: Design and Analysis.* Springer Singapore, 2017.

[22] V.D. Colli, P. Cancelliere, F. Marignetti, R. Di Stefano, and M. Scarano. A tubular-generator drive for wave energy conversion. *IEEE Transactions on Industrial Electronics*, 53:1152–1159, 2006.

[23] M. A. F. M. Hamim, T. Ibrahim, and N. M. Nor. Modeling of a tubular permanent magnet linear generator for wave energy conversion using finite element method. *2014 5th International Conference on Intelligent and Advanced Systems (ICIAS)*, pages 1–5, 2014.

[24] Hew Wooi Ping, Hamzah Arof, and Wijono. Design of a permanent magnet linear generator. *2006 International Forum on Strategic Technology*, pages 231–234, 2006.

[25] Jawad Faiz, Mahdi Ebrahimi-Salari, and Gh. Shahgholian. Reduction of cogging force in linear permanent-magnet generators. *IEEE Transactions on Magnetics*, 46:135–140, 2010.

[26] Jawad Faiz and Alireza Nematsaberi. Linear permanent magnet generator concepts for direct-drive wave energy converters: A comprehensive review. In *2017 12th IEEE Conference on Industrial Electronics and Applications (ICIEA)*, pages 618–623, 2017.

[27] Dan Li, Baodong Bai, Qing Yu, and Dezhi Chen. Cogging force minimization in a permanent magnet linear generator for sea wave energy extraction applications. In *2009 International Conference on Energy and Environment Technology*, volume 1, pages 552–554, 2009.

[28] Joseph Prudell, Martin Stoddard, Ean Amon, Ted K. A. Brekken, and Annette von Jouanne. A permanent-magnet tubular linear generator for ocean wave energy conversion. *IEEE Transactions on Industry Applications*, 46(6):2392–2400, 2010.

[29] Amal Souissi, Imen Abdennadher, and Ahmed Masmoudi. Investigation of the effects of the pole shoe geometry on the ipm t-lsm features: Application to free piston engines. *IEEE Access*, 10:17748–17759, 2022.

[30] Einar Halvorsen, Cuong Le, P. Mitcheson, and Eric Yeatman. Architecture-independent power bound for vibration energy harvesters. *Journal of Physics Conference Series*, 476:2026–, 12 2013.

[31] A. H. Hosseinloo. *Nonlinear Vibration Energy Harvesting: fundamental limits, robustness issues, and practical approaches*. PhD dissertation, Massachusetts Institute of Technology, Department of Mechanical Engineering, 2018.

[32] Yu Jia. Review of nonlinear vibration energy harvesting: Duffing, bistability, parametric, stochastic and others. *Journal of Intelligent Material Systems and Structures*, 31:921–944, 2020.